Investigation of inner-outer interactions in a turbulent boundary layer using high-speed particle image velocimetry

Gokul Pathikonda and Kenneth T. Christensen

Phys. Rev. Fluids **4**, 034607 — Published 29 March 2019

DOI: 10.1103/PhysRevFluids.4.034607

Investigation of inner–outer interactions in a turbulent boundary layer using high-speed PIV

Gokul Pathikonda*
Department of Mechanical Science and Engineering,
University of Illinois, Urbana-Champaign and
Aerospace and Mechanical Engineering,
University of Notre Dame, Notre Dame, IN, USA

Kenneth T. Christensen†
Aerospace & Mechanical Engineering,
Civil & Environmental Engineering & Earth Sciences,
University of Notre Dame, Notre Dame, IN USA and
International Institute for Carbon-Neutral Energy Research,
Kyushu University, Fukuoka, Japan

Abstract

The structure of inner–outer interactions in a smooth-wall turbulent boundary layer was investigated using high frame-rate PIV with two, overlapping fields of view. A refractive index-matched (RIM) facility was used to enable the resolution of turbulent structures very close to the wall where these modulation effects are dominant. Amplitude and frequency modulation correlation coefficients were first investigated by computing single-, two- and multi-point correlation analyses now routinely reported in the literature. The wall-normal trends in amplitude modulation for the streamwise and wall-normal velocities, and in frequency modulation for the streamwise velocity, are consistent with that previously reported in literature, validating the efficacy of the PIV approached used herein. The frequency modulation behavior for wall-normal velocity, however, differed from its amplitude modulation counterpart in the near-wall region. As this is the first study to report frequency modulation results for the wall-normal velocity, it is not clear whether this difference is physical or a byproduct of enhanced sensitivity to measurement noise and/or finite spatial resolution of the measurements. Leveraging the spatial and temporal nature of the PIV data, a conditional average-based method was extended to the PIV data to directly capture the spatio–temporal signature of these interactions. This spatio–temporal picture revealed that the small-scale variance in streamwise and wall-normal velocity fluctuations not only correlates with the slow variations of the large scales in the logarithmic region, but it also leads the local large scales (measured using a single hot-wire, for example). These observations clearly indicate a structure akin to that proposed in Baars *et al.* [Exp Fluids, 56:188 (2015)], including the relative positions of the modulated and modulating scales. The independence of these observations with filter choice is also shown, with equivalent correlation coefficients developed based on the conditional averaging analysis.

---

[*] Present address: The George W. Woodruff School of Mechanical Engineering, Georgia Institute of Technology

[†] christensen.33@nd.edu

I. INTRODUCTION

The canonical incompressible smooth-wall turbulent boundary layer at high Reynolds numbers (*Re*) has been investigated for over 100 years, with much of the interest stemming from its ubiquity in engineering and physical phenomena. The turbulent physics within the boundary layer is responsible for important interactions between the free-stream flow and the surface, such as surface drag, dissipation, heat transfer, etc. While the utility of accurately understanding the turbulent interactions that occur in this thin region cannot be overstated, the flow involves a high degree of non-linearity and a challenging range of spatial and temporal scales. This complexity grows with increasing *Re*, quickly placing direct investigation of all scales in a typical real-world application well away from existing theoretical, computational and experimental capabilities [2, 3]. The turbulent boundary layer develops distinct regions of dominant physics that are separated spatially and spectrally. For example, a 'near-wall' region forms and becomes increasingly smaller in physical extent with *Re* and contains within it the dominant viscous effects, while the outer region is driven by inertial effects and is momentum dominant. This broad range of scales causes challenges despite many advances on the technological and computational fronts [4], (we discuss one aspect in §I B). Thus, the most appropriate way to understand and predict real-world turbulent boundary layers has been via scaling laws and extrapolating models that are developed from low to moderate *Re* studies to higher ones (such as Clauser [5]).

This practice, however, requires an accurate understanding of all relevant turbulent phenomena, and their *Re*-scaling. While these scaling laws and extrapolations can be very useful, today's advanced computational and experimental efforts are constantly unearthing new physics that occur predominantly at higher *Re*. The presence of large- and meandering very large-scale motions [6], attached eddy/hairpin vortex structures [7], high- and low-momentum regions [8], evolution of an outer turbulence peak [9] etc. are a few examples to this end. These high *Re* physics and their *Re*-dependence must be captured, understood and accurately modeled to transform our current predictive capabilities.

To this end, one of the most promising recent insights regarding wall turbulence is the observation and quantification of inner–outer interactions at high *Re* [10]. With increasing *Re*, the large- and very large-scale motions become an increasingly influential component of the flow, while simultaneously developing (by definition of high *Re*) a large temporal and spatial scale separation between them and the small scales that occupy the near-wall region. Mathis *et al.* [10] identified amplitude and frequency (and possibly scale) modulations of the latter by the former. This amplitude modulation was also observed in wall skin friction traces, indicating the engineering significance of these interactions. These modulation interactions highlight the presence of turbulent phenomena that are increasingly dominant with *Re*, and that must be understood to realize effective models for use in real-world applications. The current work is a part of this recent interest to observe, define and better understand this phenomena so as to lead to improved predictive capabilities of flows involving high *Re* turbulent boundary layers.

A. Inner–outer modulation interactions

The notion of interactions between the large scales in the outer layer and the small scales near the wall has been considered for some time. The frequency of near-wall turbulent 'bursts' (resulting in spontaneous ejection of high turbulence intensity away from wall) has been observed to scale with *Re*, despite the hypothesized autonomy and *Re*-independence of near-wall dynamics [11]. Bandyopadhyay and Hussain [12] observed a strong coupling between the intensity of small scales and the local large scales, indicating a modulating interaction between them. Further development of advanced diagnostic techniques such as PIV and post-processing computational power led to the observation of coherent turbulent structures termed 'hairpin vortices' that fit very well with the previous attached eddy hypotheses [7, 13, 14]. A statistical description of these instantaneous structures showed them to be dominant carriers of Reynolds stresses in the flow, highlighting their significance in boundary-layer flow physics [8, 15, 16]. These hairpin vortices appeared to form coherent packets leading to energy residing at large ($\sim \delta$) and very large scales ($> 3\delta$), the latter meandering in the spanwise direction as they are convected by the mean flow [6, 8, 9, 17, 18]. Hutchins and Marusic [19] first observed the influence of these meandering structures from the outer layer to the near-wall region and hypothesized a 'modulating' effect of the same on the near-wall flow physics. These interactions were quantified more definitively by Mathis *et al.* [10] who proposed a metric to show the amplitude modulation (AM) of near-wall streamwise velocity scales by the outer larger scales, and the effect of *Re* on the same. The observation of AM of spanwise and wall-normal velocity fluctuations [20] and skin-friction fluctuations [21] corroborated this modulation effect and its significance. A simple and effective model was proposed by Mathis *et al.* [22] and Marusic *et al.* [23] to quantify this effect and to predict near-wall turbulence statistics, which was extended further by Baars *et al.* [24] using linear stochastic estimation. For the remainder of the current work, we shall refer to this phenomena as 'inner–outer interactions (IOIs)', with a comprehensive review of the same and the modeling presented in [25].

More recently, Bernardini and Pirozzoli [26] presented evidence of AM in channel flows from DNS data, while Mathis *et al.* [27] and Duvvuri and McKeon [28] deconstructed the AM correlation coefficient as a component of skewness of turbulent velocity fluctuations. Guala *et al.* [29] investigated the atmospheric boundary layer at very high Re and identified the presence of AM interactions via correlations and conditional averages. Chung and McKeon [30] and Hutchins *et al.* [31], using LES and experiments, respectively, at high Re and conditional averages, established a relation between the wall-parallel gradients of large-scale velocity and the small-scale fluctuations, helping to clarify the spatial structure of these interactions.

These IOIs have also been observed as frequency modulations of the near-wall scales by the outer large scales. Ganapathisubramani *et al.* [32] and Baars *et al.* [1] identified and quantified the same using conditional analysis and wavelet power spectra, respectively. The robustness of these modulations has also been identified as they also exist in flows over rough walls [33–37, etc.], in flows embodying synthetic large scales [28, 38], in boundary layers subjected to pressure gradients [39], and other flow configurations [40, 41], etc. These phenomena were also shown computationally using DNS [26, 42] and LES [43–45]. With these interactions in mind, and the already-shown ability to model near-wall turbulence statistics based on these interactions [22, 23], the development of subgrid-scale (SGS) models for LES of high-Re based on these concepts is intriguing since it is the larger scales that are resolved in LES. Recent work of Wu *et al.* [42] extended the use of principle component analysis to develop predictive models using highly resolved DNS of a transitionally-rough channel flow, and to successfully predict up to fourth-order turbulence statistics, including cross terms involving all three velocity components, based on an AM model. Sidebottom *et al.* [43] proposed the same based on modulation interactions, which were employed by further simulations over smooth and rough walls by Anderson [44], Awasthi and Anderson [45].

Recent studies have proposed frameworks to explain this high *Re* phenomena. Chernyshenko *et al.* [46] and Zhang and Chernyshenko [47] described this effect as a quasi-steady, quasi-homogenous (QSQH) phenomena at high *Re* owing to the large separation in spatial and temporal scales of evolution between the interacting structures. In particular, the near-wall scales are extremely 'small' and evolve 'fast' relative to the 'large and slow' outer scales, hence responding to the latter as a slow variation in instantaneous *Re*. At high *Re*, this description extends hypothesized universality in the near-wall physics by a slow QSQH variation of *Re*. More recently, Chernyshenko *et al.* [48] proposed an appropriate filter to decouple these small and large scales from each other for this purpose. Other descriptions have also been proposed using Hölder exponents [49] and resolvent mode analyses [50]. The latter description provides a spatio–temporal framework of these interactions as an inclined large scale convecting with small scales correlated in amplitude and frequency, and lagging in space and time. This description is further supported from Taylor's hypothesis-based reconstructions of high-temporal resolution point measurements and conditional averages/correlations [24, 31, 34] for flow over smooth and rough walls. Finally, Hu and Zheng [51], using novel decompositions to separate 'turbulence inner-only scales' from the outer scales, revealed the clear existence of energetic outer large scales at much lower Re_τ than previously thought. These new observations help explain the identification of clear modulation effects at *Re* [26, for eg., $Re_\tau \approx 1100$] lower than that for which a clear signature of energetic, outer-layer large scales is evident in un-decomposed spectrograms of streamwise turbulent kinetic energy.

Given the significance of IOIs in the evolution of wall turbulence, it is crucial to gain a better understanding of the physics and mechanics responsible for the same. As already discussed, several studies have experimentally studied these interactions using high-frequency, point-wise velocity or shear-stress measurements and high spatial-resolution, though temporally uncorrelated, PIV measurements [52] to establish aspects of the spatial structure of these interactions. The current work is an attempt to more fully explore these interactions, where a smooth-wall turbulent boundary layer is examined using high temporal-resolution PIV to examine IOIs in a true spatio–temporal sense. With optimized spatial and temporal resolutions that capture the requisite time and length scales, these unique datasets enable not only the study of amplitude and frequency modulation using temporal-only analysis, but also the use of conditional averaging techniques for a more complete spatio–temporal picture of these interactions. Further, the availability of high-speed and high-resolution wall-normal velocity data enables the investigation these interactions through the wall-normal turbulence. With the use of refractive-index matching (RIM) and careful qualification of the diagnostics, we attempt to gain new perspectives on the spatial structure of IOIs and their evolution.

B. Challenges of capturing inner–outer interactions with PIV

The dynamic range of spatial and temporal scales of high-Re wall turbulence poses significant challenges in both computational and experimental research. Consider a typical academic smooth-wall turbulent boundary layer in a wind tunnel of $Re_\tau \sim 5000$ and $\delta \sim 100\,\mathrm{mm}$ [34]. The smallest scales are $\sim 25\,\mu\mathrm{m}$ and the largest scales are $\sim 1\,\mathrm{m}$, while the smallest and largest time scales are $\sim 50\,\mu\mathrm{s}$ and $\sim 100\,\mathrm{ms}$, respectively. To realize a complete spatio–temporal measure of such a boundary layer using planar PIV, one requires cameras with resolutions of order $\sim 100,000 \times 100,000\,\mathrm{px}^2$ that can acquire images at $\sim 10\,\mathrm{kHz}$. These requirements are prohibitively impractical, not only in terms of technology required but also the data processing and post-processing capabilities that such data would demand. These limitations further highlight the advantages of hot-wire anemometry in studying high-Re boundary layers via very-high dynamic range, albeit point-wise, measurements. It is thus evident that replicating high frame-rate PIV as an equivalent array of hot-wire sensors is highly impractical.

The investigation of IOIs via PIV poses further challenges. Much of the turbulent modulation occurs close to the wall ($y^+ \sim 20 - 50$, [1, 10, 34]) where small scales are rich and can respond to the larger scales in a quasi-steady, quasi-homogenous sense. With increasing Re, for a given physical experimental facility, this inner region occupies an increasingly smaller physical extent in the boundary layer. For example, in a boundary layer that is $\sim 100\,\mathrm{mm}$ thick, at $Re_\tau \approx 2000$, the near-wall peak in $\langle u^{2+} \rangle$ is physically located around $\sim 750\,\mu\mathrm{m}$. The same dynamics in $Re_\tau \approx 5000$ in a wind-tunnel facility would see the turbulent peak move to $\sim 370\,\mu\mathrm{m}$. While this can be readily measured with a typical hot-wire sensor given the extremely small sensor sizes ($\sim 2 - 5\,\mu\mathrm{m}$) relative to the boundary-layer structures, it is extremely difficult to resolve the same with a typical PIV interrogation window of $\sim 200\,\mu\mathrm{m}$. Further, PIV involves volumetric averaging over a much larger volume [typically

$O(100\,\mu\mathrm{m}) \times O(100\,\mu\mathrm{m}) \times O(1\,\mathrm{mm}$ in sheet thickness)], which causes significant attenuation of small-scale energy compared to hot-wire sensors [typically $O(5\,\mu\mathrm{m}) \times O(5\,\mu\mathrm{m}) \times O(1\,\mathrm{mm}$ in wire length)]. For this reason, PIV performs best in resolving small-scale energy in a streamwise–wall-normal configuration (where bulk-averaging, $O(1\,\mathrm{mm})$, occurs in the spanwise direction), compared to streamwise–spanwise or spanwise–wall-normal planes (where bulk averaging, $O(1\,\mathrm{mm})$, occurs in the wall-normal or streamwise directions, respectively). Decreasing the Re_τ does not necessarily alleviate this issue, as the associated IOIs also become weaker at lower Re [10, 27]. Beyond issues of spatial resolution, PIV suffers from other challenges when one tries to measure too close to the wall, such as low seeding density and correlation biases due to high shear in the flow as well as finite wall-normal extent of the PIV interrogation spot size. One potential solution to these challenges is to increase the scale of the experiments, such as the High Reynolds Number Boundary Layer Wind Tunnel (HRNBLWT, [53]), the Princeton 'Superpipe' [54], the Flow Physics Facility at New Hampshire [55], CICLoPE [56], or to perform experiments on the atmospheric boundary layer, such as [57]. But otherwise left to the confines of a given experimental facility, it is thus an optimization problem of decreasing the Re_τ to be able to capture the near-wall physics using PIV, and having significant enough modulation interactions to be captured.

Fortunately, significant physical understanding can be gained by leveraging a few justifiable assumptions, even within the limitations of PIV technology and experimental facilities. Recent studies [26, 42] at lower Re_τ revealed the presence of strong modulation coefficients in the flow, even when a dominant outer peak in pre-multiplied streamwise turbulence spectra is not significant (though an outer peak is more readily observable in spanwise spectra). The recent work of Hu and Zheng [51] helps explain the occurrence of such modulation at lower Re. Using advanced decompositions to separate 'turbulence inner-only scales' from the outer scales, Hu and Zheng [51] revealed more clearly the presence of energetic outer large-scale structures at much lower Re_τ than previously thought. From a PIV standpoint, this new evidence reduces the spatio–temporal resolution requirements by allowing a moderate Re_τ to be studied as a means of assessing its ability to capture the modulation of the near-wall flow by outer large scales. Further, Taylor's hypothesis can still be used to estimate the large- and very large-scale motions (that are much longer than typical PIV fields of view) from a sufficiently long PIV time series [58, 59]. The utility of this approach will also be seen in the current work (§IV B). Care must to be taken during experiments to minimize near-wall reflections, maximize the vector quality close to the wall, and satisfactorily deal with spurious vectors. The use of refractive-index matching greatly improves data yield in the near-wall region, particularly in rough-wall flows, by greatly reducing near-wall reflections of laser light. The following sections describe the experiments performed, the flow characteristics, and various tools used to investigate the inner–outer interactions to the confines of these constraints.

To this end, high-frame-rate PIV measurements were made in a turbulent boundary layer formed in a unique refractive-index-matching flow facility. A dual field-of-view approach was utilized to ensure sufficient spatial resolution to capture the small scales with a smaller field of view while simultaneously ensuring capture of the larger scales with a wider streamwise field of view. This data is used to explore the utility of high-frame-rate PIV in quantifying IOIs in wall turbulence and is leveraged to highlight key aspects of the spatio–temporal structure of these interactions that is only achievable with temporally resolved data that retains multipoint information about the flow (i.e., spatially resolved velocity fields in the case of PIV).

II. EXPERIMENTS

A. Refractive Index-Matching (RIM) and High Speed PIV

All experiments were performed in a RIM flow facility at the University of Notre Dame – a closed loop liquid facility, operated by a 7.5 HP centrifugal pump. From the pump, the flow passes through a honeycomb, a series of screens and a converging section before entering the test section. An in-line heat-exchanger in the flow loop, controlled by a thermostat, is operated by cold tap water to maintain the temperature of the solution at 20°C. The test section is 2.5 m long from entry to exit, has a square cross-section of side 112 mm, and is made of clear acrylic (Refractive index, RI $= 1.49$). A blanket of nitrogen is sustained over the working solution and is necessary to avoid oxidation and discoloration of the working solution [60]. The entire facility has a functioning volume of 250 liters of the working fluid. Figure 1 presents the current experimental arrangement, including a view of the RIM test section in figure 1(b).

The working solution for the facility is an aqueous solution of sodium iodide (NaI), with

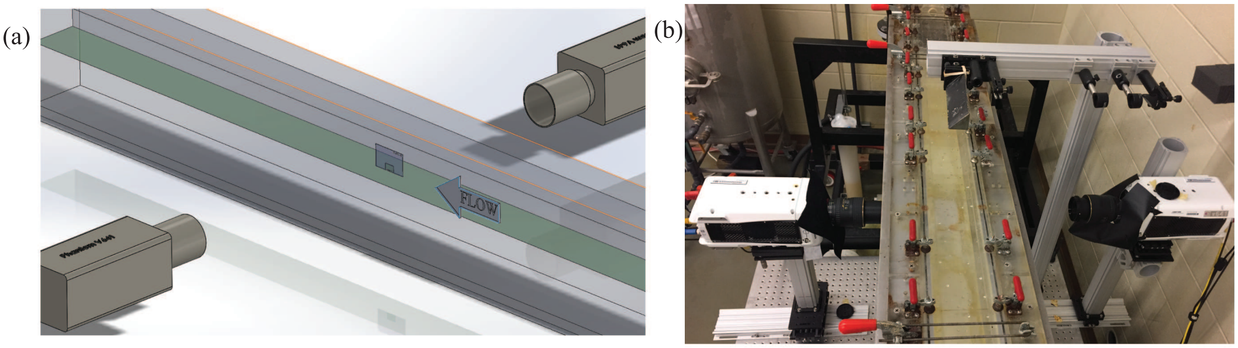

FIG. 1. (a) Schematic of the two-FOV PIV camera arrangement (floor is indicated in *green*). (b) Photo highlighting this experimental arrangement in the RIM flow facility.

a refractive index (RI) of 1.491, which matches that of the acrylic test section and the test-section floor. At these operating conditions, the specific gravity ($\bar{s}$) and kinematic viscosity (ν) of the working solution are 1.78 and $1.21 \times 10^{-6}\,\mathrm{m}^2/\mathrm{s}$, respectively. Matching the RI of the working solution with that of the test section floor avoids strong near-wall reflections of the laser sheet which typically plague near-wall PIV measurements in wall-normal planes. This approach thus enables investigation of the velocity scales within the buffer layer down to the viscous sub-layer without being hindered by wall reflections. Doing so is particularly crucial for the analysis herein as much of the modulation interactions occur very close to the wall (as detailed earlier in section I B) in smooth and rough walls [35, 61].

The high-frame-rate PIV measurements were made using a two-camera, two field of view (FOV) setup, the relative arrangement of which is shown in figure 1. This arrangement ensures that the small scales near the wall and the large scales in the outer layer are adequately captured by the PIV measurements. Two high-speed, Phantom V641 cameras were used and operated in a synchronized mode at full resolution, but different magnifications associated with the two FOVs. The cameras are equipped with full-frame, CMOS sensors with a maximum resolution of $2560 \times 1600\,\mathrm{px}^2$ (4 MP), and a 6 Gpx/sec throughput at 12 bit resolution. With these parameters, a maximum frame rate of 1450 frames/s, or 725 vector-fields/s, is achievable when operated at full resolution PIV-mode. The 32 GB on-board memory limited the duration of each continuous PIV time-series to 2734 vector-fields/s/camera (5468 images, $\sim 3.9\,\mathrm{s}$ at full frame rate), after which the images were saved to external storage before a new continuous PIV time series could be captured. Multiple time series of this length were taken to ensure as large an ensemble of data as possible to compute the necessary statistics.

A Northrop Grumman ‘Patara’ PA-050 laser was used to generate a light sheet of thickness $\sim 1\,\mathrm{mm}$ for the high-frame-rate PIV measurements. It is a high-speed, dual-cavity, Nd:YLF laser, and is capable of emitting 528 nm *green* light with an energy up to 54 mJ/pulse/cavity at pulse rates from 20 Hz to 1 kHz. A LaVision high-speed timing controller was used to control the image acquisition, synchronization and laser emission. Silver-coated solid glass spheres with a nominal diameter $2\,\mu\mathrm{m}$ were used as PIV tracer particles which have been shown to serve as effective seed particles in this RIM flow environment [62, 63]. All PIV processing was performed using Davis 8.1.3 from LaVision.

The two cameras have FOV dimensions of approximately $80 \times 50\,\mathrm{mm}^2$ and $28 \times 15\,\mathrm{mm}^2$ in the streamwise–wall-normal plane, and are henceforth referred to as, respectively, bFOV and sFOV images, vector fields etc. The sFOV was designed to capture and resolve small scales effectively in the near-wall region, while the bFOV was designed to capture a greater streamwise extent of the large scales in the outer layer as well as the bulk boundary-layer parameters. The two cameras viewed the measurement plane from opposite sides of the laser sheet in a normal (perpendicular) arrangement, but acquired images simultaneously.

Shown in figure 2 are sample instantaneous velocity fields from the sFOV and bFOV at the same time instant, illustrating the accuracy of the calibration and processing procedure as well as the excellent agreement between the measurements of the two cameras. The inset in the figure shows the difference between the two measurements in the overlapping domain, which is found to be always less than 0.08 m/s (out of a 1.07 m/s free stream velocity), and on average much smaller than this. The largest discrepancies occur close to the wall, where the sFOV PIV system has a higher fidelity in capturing the flow structures compared to the bFOV.

B. Current Flow and Measurements

All smooth-wall experiments were performed along the bottom wall of the test section at its spanwise center to minimize any side-wall effects. A 4 mm cylindrical trip attached at the entry section tripped the incoming flow after the converging section. The boundary layer developed spatially to $\approx 2\,m(\sim 50\delta)$ from the trip, before reaching the measurement section. All experiments were run at a pump speed of $20\,Hz$, which gave a free stream velocity of $U_\infty = 1.07\,\mathrm{m/s}$.

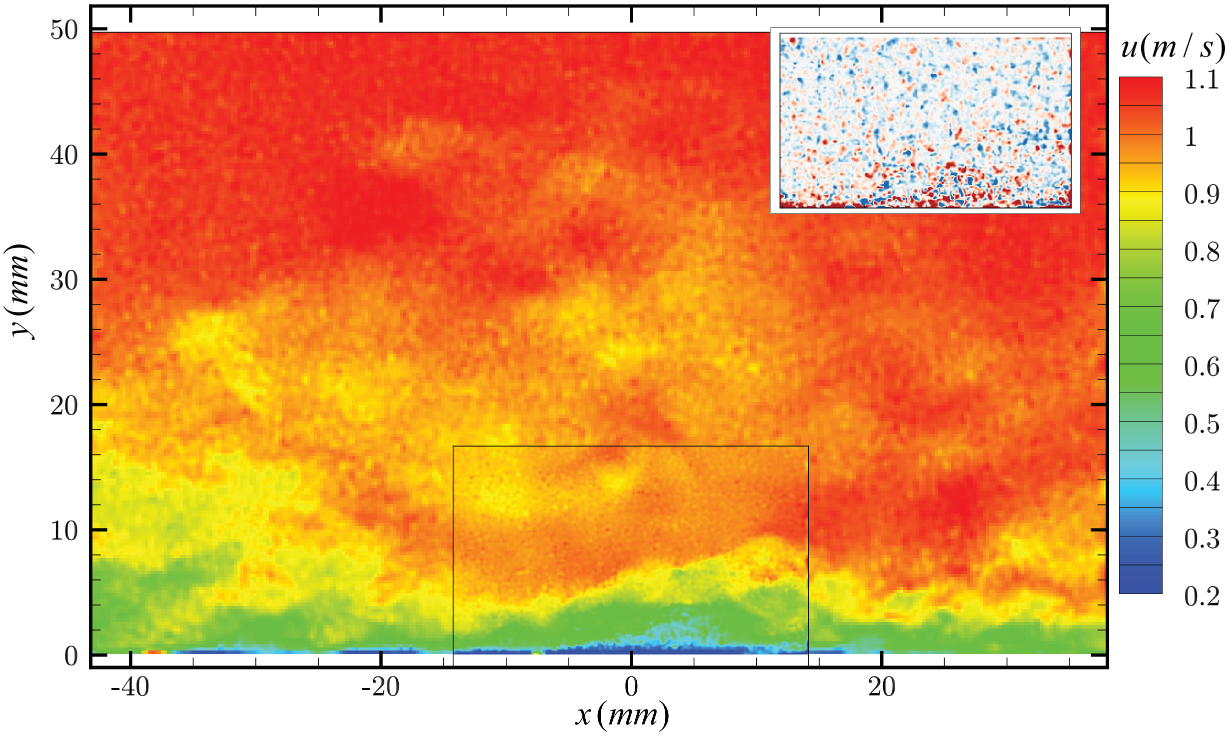

FIG. 2. An example instantaneous snapshot of streamwise velocity contours from the two cameras. The small camera (sFOV) is embedded inside the big camera (bFOV) near the wall. Also shown in inset is the velocity difference between the two cameras within the sFOV (contours ranging from -0.04 m/s (red) to 0.04 m/s (blue).

Given the dimensions and resolutions of the bFOV and sFOV, the final interrogation-spot sizes ($16 \times 16\,\mathrm{px}^2$ in both, 50% overlap) yielded a physical vector spacing of about $250\,\mu$m and $90\,\mu$m, respectively, in each linear dimension. It should be noted that the resolution of the smallest scales, however, depends on the interrogation window shape and weighting functions used. Both cameras were operated synchronously to capture vector fields at the same time instants. First, low sampling-rate data set was acquired at $F_s = 20\,Hz$ (i.e., 20 vector fields per second). This data was processed to obtain the various parameters required to characterize the turbulent boundary layer. Care was taken during processing of the images to ensure that the velocity vectors were correctly processed along the axes parallel to and perpendicular to the wall. To ensure this consistency, individual PIV images were rotated ($\sim 0.25°$) prior to processing when necessary. Due to the use of RIM, the wall

TABLE I. Measurement and flow parameters of RIM turbulent boundary layer experiments.

Label	`S20-20`	`S20-700`
Pump Speed	20 Hz	20 Hz
Vector fields per second	20 Hz ($0.72\,U_\infty/\delta$)	700 Hz ($0.43\,u_\tau/y^*$)
No. datasets	1	20
Vector fields per dataset	1000	2734
Free-stream velocity (U_∞)	1.07 m/s	
Boundary layer thickness (δ)	38 mm	
Kármán number (Re_τ)	1410	
Skin-friction velocity (u_τ)	0.045 m/s	
Viscous length scale (y^*)	27 μm	
Viscous time scale (t^*)	610 μs	
Spatial Resolution (Δx)	$6.6\,y^*$ ($sFOV$); $18.8\,y^*$ ($bFOV$)	

manifested as a very thin line of width 3 px ($\sim 30\,\mu$m) at most in the PIV images, the center of which was consistently selected as the origin for the wall. Finally, a sliding background subtraction ($20 \times 20\,px^2$) and a min–max particle intensity normalization (15×15 px^2) was applied to enhance the particle signal.

The low sampling rate ($F_s\delta/U_\infty = 0.72$) gave a larger number of uncorrelated boundary-layer snapshots, and thus served as a suitable ensemble to compute various boundary-layer parameters and statistics. One-thousand vector fields were sampled at this sampling rate, and this case is henceforth referred to as `S20-20`. This ensemble was processed using methods described earlier, ensemble averaged first, and then line averaged in the streamwise direction to improve the ensemble (i.e. assuming streamwise homogeneity). The boundary-layer parameters were extracted using the best non-linear regression fit to a theoretical form [64], with the fitted parameters giving the 'true' boundary-layer thickness ($\tilde{\delta}$), wake parameter (Π), skin friction velocity (u_τ), and a small wall correction (y_c). Kármán constant (κ) and intercept (C) of logarithmic profile were chosen to be 0.384 and 4.17, respectively. Table I summarizes the boundary-layer parameters computed from the `S20-20` dataset. In this context, the PIV interrogation spot size is $(6.6y^*)^2$ and $(18.8y^*)^2$ for the sFOV and bFOV respectively, and a laser sheet thickness is $\sim 37y^*$.

After characterizing the smooth-wall boundary layer with the low-frame-rate data, high-frame-rate PIV measurements were performed to resolve the time-dependent dynamics of the flow. For these experiments, 2,734 ($\equiv$ one camera memory) time-correlated PIV snapshots per dataset were acquired at 700 Hz (700 vector fields per second) for a duration of $\approx 3.9\,\mathrm{s}$. In flow units, this gave a time series with a temporal resolution of $2.35\,y^*/u_\tau$, with a duration of $109\,\delta/U_\infty$. This time series is sufficient to resolve the small-scale activity, and for correlations over multiple LSM and VLSM structures [typically $O(10\,\delta)$]. Twenty such datasets were collected to have an ensemble time series $\equiv 2,200\,\delta/U_\infty$, with a total of 54,680 vector-fields per FOV. These data sets are collectively referred to henceforth as `S20-700`. Table I summarizes details of the data acquired.

III. SINGLE-POINT STATISTICS

A. Mean and Turbulent Statistics

As noted earlier, the `S20-20` data was used to characterize and validate the boundary layer before general conclusions regarding IOIs were drawn from the current measurements. Investigating amplitude and frequency modulation requires one to accurately capture third-order moments of turbulent velocity fluctuations very close to the wall [27].

Figure 3 presents wall-normal profiles of the mean velocity (U), in-plane Reynolds shear stresses ($\overline{u^2}$, $\overline{v^2}$, $\overline{uv}$), and skewness of streamwise velocity ($\overline{u^3}$). These values are computed from the `S20-20` ensemble in the two FOVs and compared with the the experimental and computational works of Örlü and Schlatter [65] and Schlatter and Örlü [66] at comparable Re. The utility of the sFOV measurements, particularly in obtaining measurements very close to the wall ($y^+ < 20$), is evident as it captures the inner peak of the streamwise Reynolds normal stress and skewness. These trends are also observed in modulation correlation coefficients (section III A), where the sFOV resolution is required to capture the same near the wall. In the outer region, the appearance of an outer peak that is representative of dominant LSMs and VLSMs in high Re_τ (> 3000, [67]) boundary layers is not evident at first glance in figure 3b. However, a number of previous studies have shown the presence of these energetic structures at lower Re_τ than the current work either using spanwise power spectra (which show LSMs and VLSMs more clearly, [26, for eg., $Re_\tau \approx 1100$]) or by using more complex decompositions of velocity scales [51]. In this latter regard, Hu and Zheng [51] proposed a decomposition based on 'turbulence-only inner motions' and identified the presence of energetic outer-layer large scales and the development of n outer peak in wall-normal profiles of streamwise turbulence intensity at Re_τ where the latter is not typically evident. This new evidence of relatively strong outer large scales agrees well with the fact that strong amplitude modulation correlation coefficients have also been previously reported at Re similar to that of the current work [26, 42, etc.]. These observations are particularly relevant to the current work because of the need to balance the spatio–temporal resolution requirements of the PIV measurements to simultaneously capture the near-wall small scales and the outer large scales as discussed in §I B.

In the wake region, the mean streamwise velocity profiles reflect a weaker wake in the current flow (smaller wake parameter, Π) compared to that of the zero-pressure-gradient turbulent boundary layer data included for comparison. This weaker wake is reflective of the slight favorable pressure gradient in the small RIM flow facility given the constant cross-sectional dimensions of the test section. This effect should, however, be limited to the wake region of the boundary layer, and we expect the near-wall physics and the modulation interactions to be unaffected by the same. Indeed, [68] studied the impact of non-zero streamwise pressure gradients on modulation effects and found that favorable pressure gradients slightly suppress such influences. Thus, any modulation identified in the current work will represent a *lower* measure of such effects compared to a true zero-pressure-gradient boundary layer. In addition, the potential impact of side-wall boundary layers in this test section has been previously addressed and found to be minimal on the canonical nature of the flow at the center span of the test section [62].

B. Amplitude and Frequency Modulation

Using only the temporal evolution of velocity extracted at a fixed position in the flow, both amplitude and frequency modulations can be explored using the same methods typically used with hot-wire data [1, 10]. Doing so provides a metric of comparison regarding the use of PIV-measured velocity time series for quantifying modulation effects. The calculation of amplitude and frequency modulation coefficients is summarized as follows:

1. 'Large'-scale time signatures were computed by capturing the velocity signatures at a

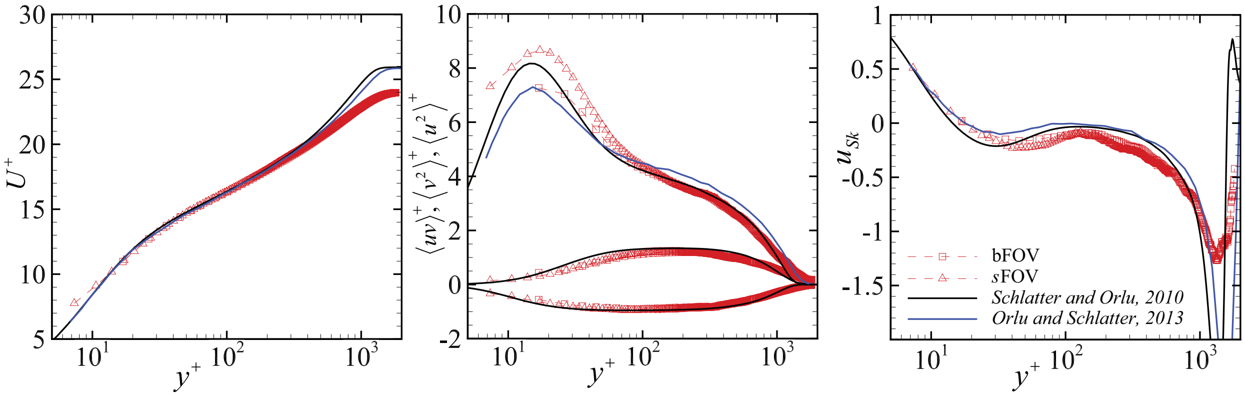

FIG. 3. Wall-normal profiles of (a) mean streamwise velocity, (b) in-plane Reynolds stresses, and (c) streamwise turbulent skewness in inner units. Profiles from the bFOV and sFOV are shown, as are LES and hot-wire results at comparable Re_τ from Schlatter and Örlü [66] and Örlü and Schlatter [65].

fixed point in the log layer, and low-pass filtering it [typically with a cutoff of $\sim O(\delta)$].

2. Similarly, the 'small' scales were identified as the high-pass-filtered velocity time traces at a point very close to the wall.

3. The 'large scale amplitude variations' of these can be computed via (1) filtered magnitude of their Hilbert transform [10] or (2) filtered integral of the wavelet spectrum at small scales [1]. The correlation coefficient between the above two signals gave the '**amplitude modulation coefficient,** R_{AM}'.

4. Similarly, the 'large scale frequency variation' was computed as a filtered 'instantaneous frequency' extracted from the wavelet power spectrum of the near-wall signature. The correlation coefficient between the large scale in step 1 and this filtered signal gave the '**frequency modulation coefficient,** R_{FM}'.

5. This step was repeated with small scales at various wall-normal positions to give the variation of these correlation coefficients as a function of wall-normal location.

6. If the large scales computed in step 1 were captured at the same location as the small scales they were correlated with, the analysis is termed '1-point analysis' as this has been previously accomplished with a single hot-wire probe at a single wall-normal position. Alternatively, if the large scales were sampled at a fixed outer location and

correlated to small scales at varying inner locations, this analysis is termed '2-point' analysis and has been previously reported from simultaneous velocity measurements from two hot-wire probes distanced in the wall-normal direction. It should be noted that the latter is a more direct measure of IOIs.

The reader is referred to the original works of Mathis *et al.* [10] and Baars *et al.* [1] for more details of these procedures. The goal of this exercise is to provide the first evidence of correlations between the large and small scales, particularly the correlation between the former and the amplitude and frequency changes of the latter. Further, using the same metrics with the two-velocity-component time series of the present measurements, modulation effects present within the wall-normal velocity fluctuations (v) are also investigated. Thus, the results of this section demonstrate the fidelity of quantifying IOIs using PIV data through the use of these metrics. To accomplish this goal, only the temporal evolution of velocity is considered (meaning all spatial information is ignored). Thus, 'large' and 'small' in the current context implies fast and slow evolution of the velocity time series in question (as with hot-wire analysis), and not their spatial variations as captured by PIV. This latter approach will be considered in §IV.

Finally, as the high-frame-rate PIV data was acquired in distinct blocks, the time series extracted from this data are in multiple, uncorrelated segments. Thus, all analysis on each time series was performed in the same way as the hot-wire analysis in [1, 10], but for one small distinction. While all averages from the hot-wire time series were typically computed via time average, the computation of the same for the current PIV data was performed via time and ensemble averaging. Doing so improved convergence of all averages.

Figure 4a presents the amplitude modulation correlation coefficient from 1-point and 2-point analyses, using Hilbert transform envelope based approach. The physical center of the log layer ($\sqrt{15Re_\tau} \approx 145y^*$, [67]) was selected as the outer position to sample the 'outer' large scales for 2-point analysis in the current discussion. The high magnitude of the correlation close to the wall for u reveals robust correlation between the large- and small-scale amplitude variations of the small scales. The two metrics– envelope based and wavelet energy based analyses – show identical results despite being rather different approaches for representing the smaller scales (not shown for brevity). This consistency confirms the equivalency of the two metrics in measuring the small-scale amplitude variations in u, and reiterates the existence of amplitude modulation in this smooth-wall flow. Further, the two-point analysis, which is a more direct measure of the amplitude modulation of the outer large scales (independently sampled) on the near-wall small scales, show even larger correlation coefficients for the u velocity component. This observation is consistent with that noted from analysis of hot-wire measurements [1, 10, 34]. Not available in the cited hot-wire measurements were time series of v. Here, analysis of v time series (figure 4b) also reveals strong amplitude modulation. These levels of modulation of the v velocity component agrees well with the observations of [20] who investigated and demonstrated the modulation of all three velocity components using multi-component hot-wire anemometry measurements. In addition, the results compare very well with the correlations reported in Wu *et al.* [42] (computed on the DNS simulations of Hoyas and Jiménez [69], channel flow at $Re_\tau = 2000$), reiterating the fidelity of the current PIV measurements. The discrepancies in the correlation values between the DNS and current experiments can be explained very well to the differences in Re_τ [10] and the choice of the outer point ($y_o^+ = 145$ in current flow versus 173 in Wu *et al.* [42]).

When simultaneous time-series data is available at multiple wall-normal positions, as is typically the case with DNS and the current PIV data, it is helpful to visualize the amplitude modulation correlation coefficients as multi-point contours, instead of one- or two-point profiles, as a complement to hot-wire observations that are not amenable to such an approach. Bernardini and Pirozzoli [26] and Eitel-Amor *et al.* [70] used this approach to identify the outer location in the log layer to which the modulation correlates best. Figure 4(c,d) shows the same for both the streamwise and wall-normal velocities, where y_i^+ refers to the wall-normal location where the small scales are sampled, and y_o^+ refers to the location where the large scales are sampled. Extracting the values on $y_i^+ = y_o^+$ line recovers the one-point correlation coefficients in figure 4(a,b), and the values along the line at $y_o^+ = 145$ recover the two-point correlation coefficients in this same figure. Further, the location of a secondary outer correlation peak close to the wall for $y_o^+ \approx 150$ in both the u- and v- correlations and its magnitude (≈ 0.3) at the current Re_τ are entirely consistent with that reported by Bernardini and Pirozzoli [26]. In particular, Bernardini and Pirozzoli [26] verified that this outer peak is a physical characteristic of the smooth-wall boundary layer they simulated via DNS by showing that this peak is absent in a synthetic signal of similar single-point statistical behavior (skewness) but lacking spatial structure.

Though consistency with previous hot-wire analyses is found, a few important distinctions

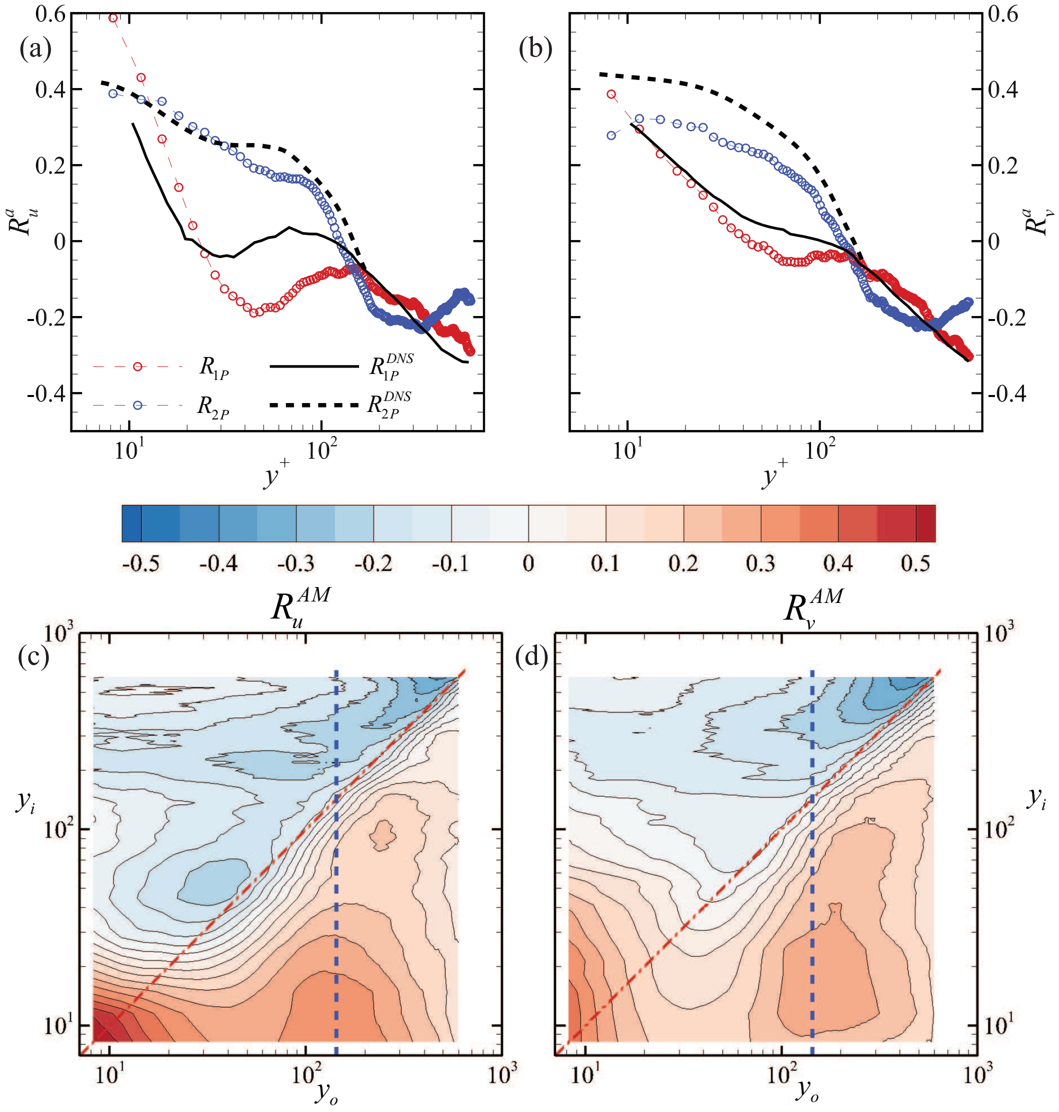

FIG. 4. (a, b) 1-point and 2-point amplitude modulation correlation coefficients based on the streamwise (left) and wall-normal (right) velocity components, respectively, using envelope-based method from sFOV. Also shown are similar coefficients from the $Re_\tau = 2000$ channel-flow DNS of Hoyas and Jiménez [69] computed by Wu *et al.* [42]. (c, d) Multi-point AM correlation coefficients for streamwise and wall-normal velocity fluctuations. *Blue* dashed line indicates 2-point correlation coefficient values, and *red* line indicates the 1-point counterparts reported in (a, b).

can also be observed in the current PIV results when compared to hot-wire analysis. Firstly, the zero-crossing of the correlation coefficient in the 1-point metric occurs much closer to the wall, with the remainder of the correlation being negative through the rest of the boundary layer. A plateau that is reported [10] at higher *Re* in the buffer region is also not present in the current correlation coefficients. These differences, we speculate, are due to the lower Re_τ in the current RIM experiments, compared to these previous wind-tunnel experiments. The same can be observed in the amplitude modulation correlation coefficients found via DNS simulations at smaller Re_τ, where the near-wall correlation peak in 1-point analysis is confined to much closer to the wall [26, 70]. This peak grows in wall-normal extent with increasing Re_τ [10], and the plateau becomes evident with corresponding increase in separation between the logarithmic and near-wall regions of the flow.

Figure 5(a,b) presents 1-point and 2-point frequency modulation correlation coefficients in u and v. The frequency modulation coefficients for u show similar behavior to that identified in the amplitude modulation coefficients. In particular, the 1-point correlation coefficient for u shows a strong peak close to the wall before becoming negative away from the wall, and the 2-point correlation coefficient for u indicates positive frequency modulation correlation coefficients. The multi-point correlation contours, shown in figure 5(c), indicate a structure similar to its amplitude modulation counterpart (figure 4c), thus confirming the presence of inner–outer interactions. The frequency modulation of the wall-normal velocity v is markedly different from its streamwise velocity counterpart as well as the amplitude modulation coefficient trends for v. Both the single- and multi-point correlation coefficients in v (figures 5b and 5d) reach a maxima in the log region and show a diminishing correlation of instantaneous frequency close to the wall. This trend can be understood by noting that v is dampened very close to the wall due to the no-penetration boundary condition. To the best of the authors' knowledge, the current study is the first, and only study so far, to investigate frequency modulation of the wall-normal velocity component, and it would be interesting to compare these observations with those from DNS or hot-wire approaches that would be better optimized for this purpose.

Important distinctions are also evident in the trends of the current frequency modulation coefficients compared to their hot-wire counterparts in Baars *et al.* [1] and Pathikonda and Christensen [34]. First, the frequency modulation of u appears weaker in the current flow as reflected by the lower values of correlation coefficient (≈ 0.2 at peak vs 0.4 from hot-wire analyses [1, 34]). Interestingly, the current frequency modulation correlation becomes negative away from the wall in one-point analysis, which is contrary to previous studies [1, 34] where the coefficient decreased to nearly zero. Further, the wall-normal velocity coefficient has a diminishing coefficient close to the wall, as reflected in the multi-point correlation maps.

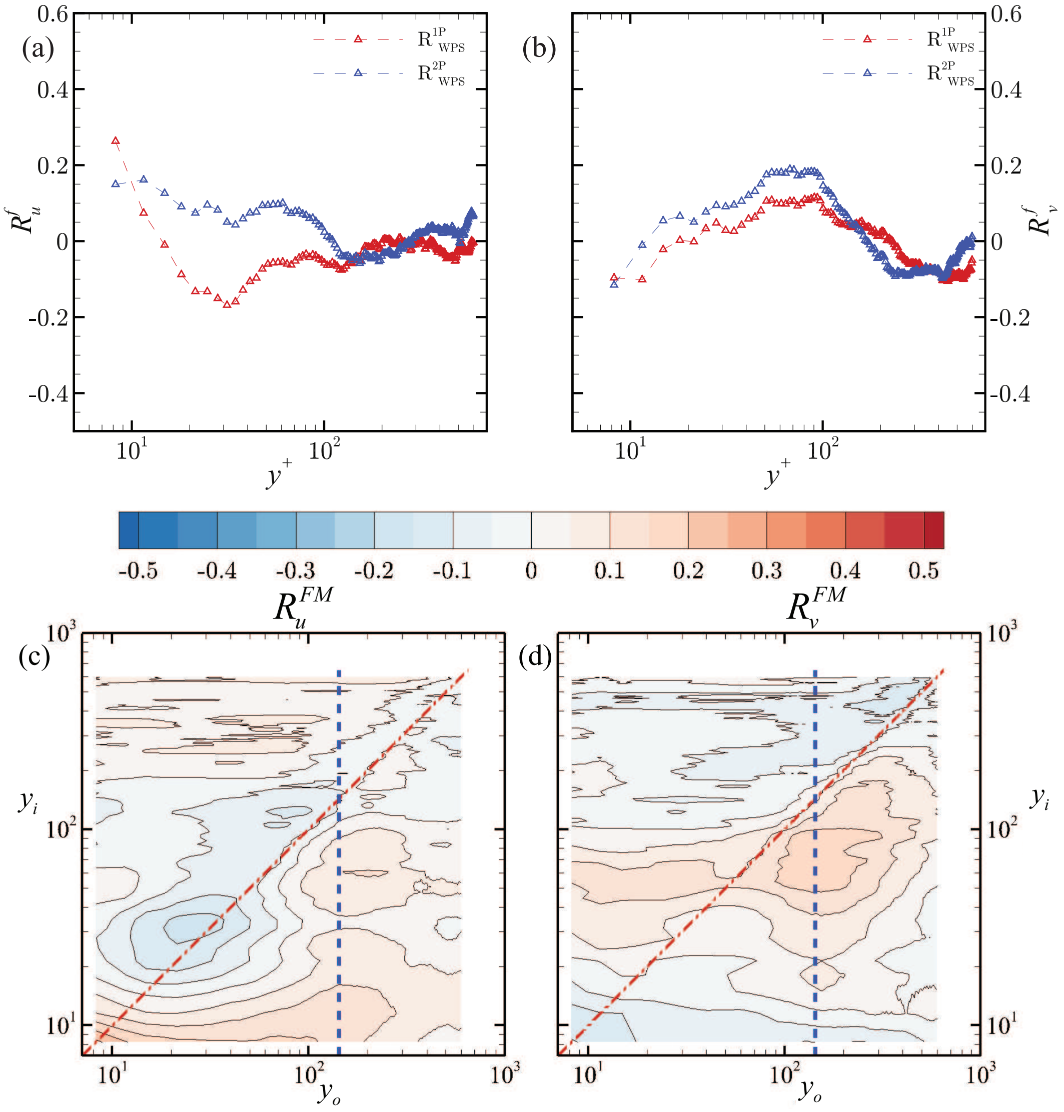

FIG. 5. (a, b) 1-point and 2-point frequency modulation correlation coefficients based on the streamwise (left) and wall-normal (right) velocity components, respectively, using wavelet-energy based method from sFOV. (c, d) Multi-point FM correlation coefficients for streamwise and wall-normal velocity components. *Blue* dashed line indicates 2-point correlation coefficient values, and *red* line indicates the counterparts reported in (a, b).

This latter observation must be taken with caution, as the diminishing correlation could be a combination of low-*Re* effects (meaning weak FM effects to begin with), no-penetration wall effects (and therefore small v magnitude) and perhaps limitations of PIV for this specific analysis (high sub-pixel error and spatial averaging in the wall-normal direction). Previous studies have shown the FM-correlation coefficient to be highly susceptible to noise in the data, unlike the AM coefficient which is more robust to noise [35]. This sensitivity has a greater impact when relatively weak $v-$velocities are measured with a finite sub-pixel resolution of the PIV system (and hence higher noise). Nevertheless, the data in figure 5 do indicate the presence of frequency modulation in the present flow using the current analysis techniques, particularly in the streamwise velocity component.

IV. SPATIO–TEMPORAL ANALYSIS OF INNER–OUTER INTERACTIONS

With the amplitude and frequency correlation coefficients examined in the previous section, the wealth of spatial information embodied in the PIV data can be leveraged to explore the spatio–temporal nature of IOIs. Besides the correlations utilized for this purpose in the previous section, conditioning the large-scale events and averaging can reveal the spatial signatures of the inner–outer interactions, along with their temporal evolution. Doing so leverages the *spatial* information captured within the PIV FOV, and thus provides even richer information on the spatial characteristics of these interactions than previously-reported hot-wire measurements. The current section aims to develop these ideas and describes the spatio–temporal tools that provide a more complete picture of these interactions.

To statistically investigate the effect of the large scales in the flow on the small scales close to the wall, we use the methods of simple conditional averaging. Conditional averaging requires one to define a ‘conditional *event*’ criterion, from which an ensemble of realizations that satisfy the event criterion can be defined from the PIV data. Single or multiple criteria can be defined based on flow or experimental quantities, such as velocity, pressure, temperature, inlet conditions etc. However, in experiments such as those presented herein where the data acquisition is exclusive of the conditional events, more complex criteria occur more rarely, and it usually requires an exponentially large ensemble of raw data to extract sufficient number of conditional events for statistical analyses. While methods such as stochastic estimation [71] are available to offset impractically large raw-data requirements to a limited extent, the current analysis does not require the same. Conditional averaging has been previously used on hot-wire signals and LES data specifically to investigate the structure of large-scale events. Ganapathisubramani *et al.* [32] used peak-counting together with averages conditioned on the magnitude of the large scale to investigate amplitude and frequency modulation. Hutchins *et al.* [31] used an array of wall shear sensors to arrive at a three-dimensional conditional large-scale structure. Baars *et al.* [1] used conditional averages based on zero crossing of large scales to compute the structure of large- and small-scale energy organization, much akin to the current work, albeit from point measurements and by applying Taylor's hypothesis. Similar analysis has also been done via LES on channel flows by Chung and McKeon [30] to identify the large scale structure and its correlation with small scales. More recent studies, such as Chernyshenko *et al.* [48] and Dogan *et al.* [72], proposed advanced filtering techniques for the large-scale–small-scale decomposition suitable for IOIs. For the present analysis, we limit ourselves to simple conditional averaging, as we extend a similar zero-crossing conditional event on the large scales. The following section describes the approach, statistical criteria and the ensemble of data thus acquired.

A. Zero-crossing conditional event

The zero-crossing conditional event is used to identify and pin the large-scale events in a time–space sense. Up to now in this work (and much of the literature on IOIs), the streamwise velocity is used as a representative measure of the outer-layer structures, and correlations have been performed on the same. In other words, the changes in the near-wall cycle have been observed in conjunction with fluctuations in streamwise velocity in the logarithmic region. Correlating various quantities pertaining to the near-wall dynamics (such as near-wall velocity envelope, frequency, skin friction, etc.) can also be performed using conditional averages, as was also explored in aforementioned earlier works. For this purpose, the conditional event considered herein is defined as the occurrence of a *'zero-crossing of a large scale at the center of log layer'*. Herein, $[\cdot]_i$ refers to an ensemble set and i refers to the i^{th} element of the set. Similarly, $\langle\cdot\rangle$ refers to the ensemble average over elements of a set, *boldface* refers to vector quantities and τ is time relative to the conditional event (t referring to absolute time). Subscripts are defined as follows: *o-outer*, *L-large*, *s-small* and + (or −)- *positive* (or *negative*) *zero-crossing* event. The following steps summarize the conditional averaging procedure for a positive zero-crossing event:

1. The large-scale temporal evolution of the streamwise velocity, u_{oL}, was extracted at a reference point, $\mathbf{x_o} = (x_o, y_o)$: the geometric center of the logarithmic region given by $y_o = \sqrt{15Re_\tau}$ [67] and at $x_o = 0$. The time series at the reference point was filtered for large scales using a cut-off filter $\lambda_c^T = 2\delta$, similar to that for the temporal-point

analysis discussed in §III B. Here, superscript T is added to the filter length definition to distinguish a temporal filter applied in a Taylor's hypothesis sense from a true spatial filter.

2. The instances $[\tau_{\mathbf{0}^+}]_{\mathbf{i}}$ where the large scale crosses from negative to positive (with time, t) were identified. These instances are referred to as the 'positive zero-crossings ($\tau_{\mathbf{0}^+}$)' of the large-scale structure, and form the conditional events for the current analysis. In other words, given a time-filtered velocity field $u_L(x_o, y_o, t)$, the conditional event is defined as

$$u_L(x_o, y_o, \tau_{0^+}) = 0$$
$$\text{and}$$
$$\frac{\mathrm{d}u_L}{\mathrm{d}t}(x_o, y_o, \tau_{0^+}) > 0$$

3. The zero-conditioned ensembles of the velocity fields in bFOV and sFOV are formed by collecting the velocity vector fields as

$$[\mathbf{u}|_{0^+}(x, y, \tau)]_i = [\mathbf{u}(x, y, \tau_{0^+} + \tau)]_i\,. \tag{1}$$

The $[\mathbf{u}|_{0^+}]_i$ ensembles around an interval (τ) from $-100t^*$ to $+100t^*$ relative to τ_{o^+} were formed. For the data collected in the current experiments, 316 positive zero-crossing events were identified and formed the ensemble for each τ.

Figure 6(a) presents a representative outer u-large scale extracted at the above-mentioned reference point (x_o, y_o). The positive zero-crossings of the large-scale signal are marked, along with the temporal neighborhood $[-100\,t^*, 100\,t^*]$ around them that are considered for the current work. For a few positive zero-crossings that occur close to each other (within $200\,t^*$ in the current case, equivalently $\sim 3\delta$ using Taylor's hypothesis), the neighborhoods overlap, and conditional instances occur repeatedly as part of multiple ensembles. Such cases were few ($\sim$3.5%), were concentrated at the edges of the conditional averages, and occurred at most in two neighboring ensembles. For this reason, and to stay true to the condition imposed, we do not impose any exceptions for such occurrences. Shown in figure 6b is the ensemble average of all zero-crossing temporal neighborhoods of large-scale signals, $\langle u_{oL}(\tau)\rangle_{\tau_{0^+}}$. The temporal neighborhood, τ, considered herein embodies an averaged crest (at $\tau_\uparrow \approx 50$) and trough (at $\tau_\downarrow \approx -50$) of the large-scale structures in the flow.

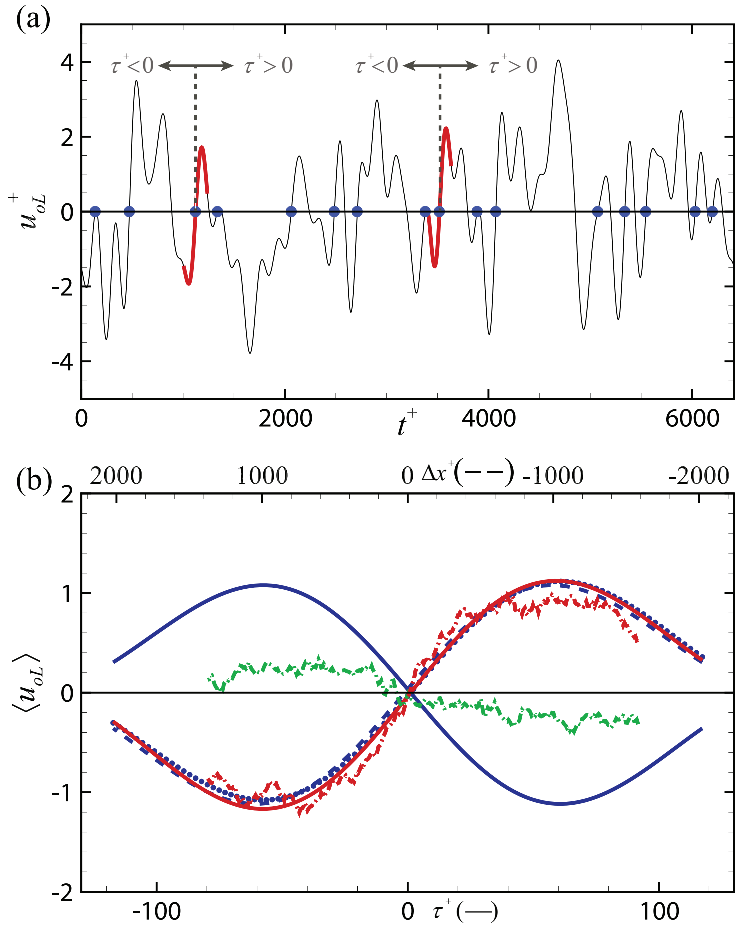

FIG. 6. (a) An example outer large-scale time series $[u_{oL}(t^+)]$, with all positive zero-crossing points (τ_{o+}) marked in *blue* dots and two example neighborhoods of width $200t^*$ in *red*. (b) The ensemble average of all such positive (*red*, $\langle u_{oL}(\tau)\rangle_{\tau_{0+}}$) and negative (*blue*, $\langle u_{oL}(\tau)\rangle_{\tau_{0-}}$, not marked in part a) zero-crossing neighborhoods. Also shown as dashed lines are ensemble averages of u- (*red*) and v- (*green*) spatial variations corresponding to τ_o^+ corresponding to Taylor's hypothesis equivalent times (i.e., $\Delta x^+ = -\tau^+ U_o$), along with $-\langle u_{oL}(\tau)\rangle_{\tau_{0-}}$ (*blue-dotted*) and $\langle u_{oL}(-\tau)\rangle_{\tau_{0-}}$ (*blue-dashed*).

The entire analysis can also be performed with a conditional event defined on negative zero-crossings of the large scale signature. Figure 6(b) shows such an averaged negative zero-crossing event of large scales, alongside its positive counterpart. As expected, the structure is symmetric about τ, with the temporal point of reference merely translated by $1/2\lambda_c^T$. Figure 6(b) also shows $-\langle u_{oL}(\tau)\rangle_{\tau_{o-}}$ and $\langle u_{oL}(-\tau)\rangle_{\tau_{o-}}$ highlighting that the conditionally-averaged structure is symmetric in magnitude around the mean and in time around the zero-crossing instant. We exploit the former symmetry to increase the ensemble of conditional fields around the zero crossing, i.e, that the conditional structure and their subsequent effects on the quantities discussed here are symmetric to the magnitude of the large scale. In other words,

$$[\mathbf{u}|_{0^+}(x,y,\tau)]_i \equiv [-\mathbf{u}|_{0^-}(x,y,\tau)]_i \,. \tag{2}$$

This equivalence was observed to be true for all quantitative trends presented in the current work [35]. From the above assumption, the ensemble of conditional events was increased to 634 fields per τ. All conditional statistics presented here were computed with this larger ensemble for better convergence. Consequently, the subscript $0c$ is used to refer to a zero-crossing event, regardless of sign.

B. Spatio–temporal footprint of the large scales

From the velocity fields in the zero-crossing conditional ensemble, the streamwise spatial footprint and the temporal evolution of the conditional event was calculated by ensemble averaging as $\langle \mathbf{u}_{0c}(x, y_o, \tau)\rangle$. Figure 6(b) compares the spatial footprint of the conditionally-averaged large scale along with the temporal average of the same, and with the spatial-to-temporal transformation accomplished using Taylor's hypothesis (i.e., $\tau \equiv -x/U_o$). This comparison reemphasizes the applicability of Taylor's hypothesis for the large convecting scales defined as in §IV A, since the two measures of the structures are essentially identical. Figure 6(b) further shows the spatial footprint of the conditionally-averaged v- velocity from the bFOV camera at $\tau^+ = 0$. The opposing signs of conditionally-averaged u and v at all times/positions is expected, since the average Reynolds shear stress component, $\langle uv\rangle$, is negative throughout the boundary layer as reflected in figure 3(b). Thus, the temporal evolution of the large scale at the reference point can be seen approximately as convection of the large scale through the reference point.

With this understanding, figure 7 presents the full spatial structure of conditionally-averaged u and v at various times relative to the the zero-crossing time instant, τ_o. The inclined structure of this conditionally-averaged velocity field is readily evident, as are the opposite signs of streamwise and wall-normal velocity fluctuations at all times. The convection of the conditionally-averaged scales is also expected with the time delay, and this large scale reflects all of the spatial characteristics typically associated with an instantaneous

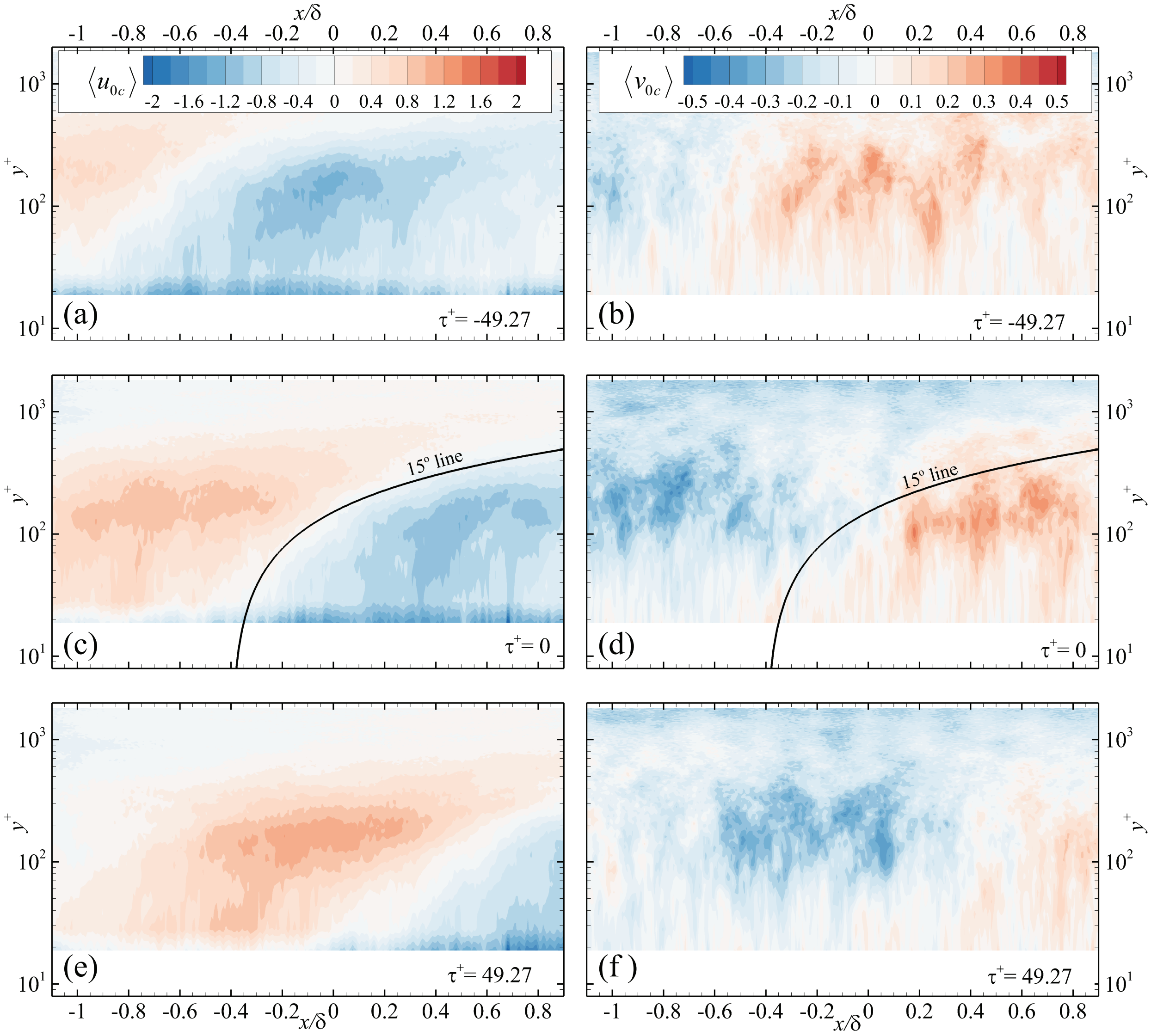

FIG. 7. (a, c, e) $\langle u \rangle_{0c}$ and (b, d, f) $\langle v \rangle_{0c}$ – the spatial signature of the large scale corresponding to $\tau = \tau_\downarrow$ (a,b), 0 (c,d) and $\tau_\uparrow$ (e,f).

large-scale motion in the streamwise–wall-normal plane, including the inclination with the horizontal of approximately 15° [7, 14, 15, 73].

To further explore the underlying modulation effects, we consider this spatio–temporal structure of conditional average for each time τ to be the corresponding measure of the large scale. That is, the filtered 'slow' fluctuations at the reference point (x_o, y_o) were used to define the conditional event. The conditional average of this ensemble of fields for each time, τ, is henceforth defined to be the "spatial signature of the large scale" for the time instant relative to the conditional event. Alternatively, the conditional averaging is equivalent to a top-hat spatial filter of filter length equal to the dimensions of the FOV (sFOV for small scales), which in the current case is equivalent to $\sim 1000\,y^*$.

C. Conditionally-averaged large-scale–small-scale organization

With the definition of the conditionally-averaged large scale given in the previous section, the small scales in each instance were extracted as

$$\mathbf{u}_L = \langle \mathbf{u}_{0c} \rangle, \tag{3}$$

$$[\mathbf{u}_s]_i = [\mathbf{u}_{0c}]_i - \mathbf{u}_L. \tag{4}$$

The variance of the small scales is used to represent the energy embodied in the small-scale turbulence for each time instant, while the ensemble average ($\langle \mathbf{u}_s^2(x, y, \tau) \rangle_i$) quantifies the mean turbulence intensity distribution and evolution for the corresponding large-scale structure. Further, to better highlight the differences in the small-scale energy content in the conditionally-averaged fields ($\equiv \langle \mathbf{u}_s^2 \rangle_i$), the small-scale energy discrepancy from the mean was computed by subtracting the unconditional intensity distribution ($\equiv \langle \mathbf{u}_s^2 \rangle_{i,\tau,x}$), and only considering the perturbation from this mean as

$$\Delta \langle \mathbf{u}_s^2 \rangle = \langle \mathbf{u}_s^2 \rangle_i - \langle \mathbf{u}_s^2 \rangle_{i,\tau,x}, \tag{5}$$

where $\langle \cdot \rangle_{i,\tau,x}$ denotes ensemble averaging, time averaging and streamwise-spatial averaging to compute the unconditional quantities on the entire ensemble of occurrences.

Figure 8 presents three time instances of the conditionally-averaged large scale, u_L (*line contours*), conditionally-averaged, small-scale variance of u, $\langle u_s^2 \rangle$ (figure 8a), and the discrepancy of the latter from the unconditioned mean, $\Delta\langle u_s^2 \rangle$ (figure 8b). Also shown is the discrepancy of the conditionally-averaged, small-scale discrepancy of v, $\Delta\langle v_s^2 \rangle$ (figure 8c). The instances chosen along columns $1-3$ correspond to $\tau = \tau_\downarrow, 0$ and $\tau_\uparrow$ respectively, and best capture the large scales and the structure of small-scale variance. A strong correlation of the large scales and the small-scale variance is clearly evident. With increasing τ, as the large scale convects from a low streamwise-momentum event ($u_{oL} < 0$) to the zero crossing event and finally towards a high streamwise-momentum event ($u_{oL} > 0$), the associated small-scale influence trails the large scales with first a decrease in small-scale variance followed by a corresponding increase in this variance. The discrepancy plots identify the

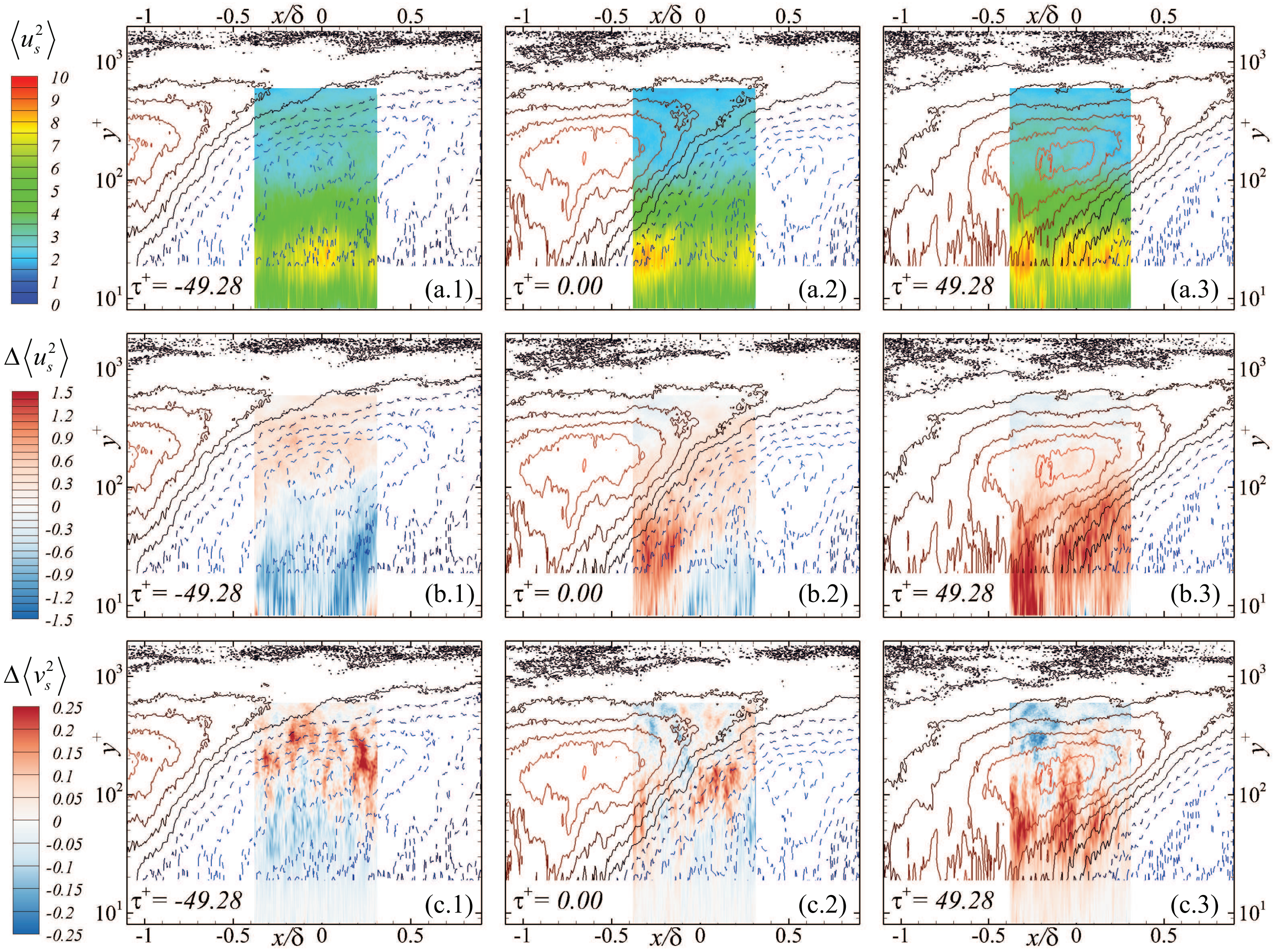

FIG. 8. Shown as filled contours are (a) small scale energy ($\langle u_s^2 \rangle$), and small scale energy discrepancy in (b) streamwise ($\Delta\langle u_s^2 \rangle$) and (c) wall-normal ($\Delta\langle v_s^2 \rangle$) turbulence at three times $(1-3)$ corresponding to $\tau = \tau_\downarrow, 0, \tau_\uparrow$ respectively. Also shown as line plots are the corresponding large scale structures u_L with same levels as shown in figure 7. Negative levels are shown as *dashed* lines. Please see video uploaded as supplemental material [76] which illustrates the full time evolution of the results presented in this figure.

location of maximum modulation effect of the small scales close to the wall, which appears to be trailing the large-scale occurrence when viewed in an Eulerian sense. More importantly, these observations directly support the conclusions drawn in our previous study of such effects in rough-wall turbulence using two-probe hot-wire measurements [34] and in the literature [1, 74, etc.], where amplitude and frequency modulation effects trail the large-scale effects in time when the latter are measured away from the wall. A similarly strong correlation, as indicated by point-temporal analysis (§III B), is reiterated in these spatial plots with regard to the wall-normal velocity as exhibited in the wall-normal variance trends (figure 8c). The small-scale, wall-normal variance also trails the modulation effects with the large scales. These observations are clear *quantitative* depictions of the spatio–temporal structure of the amplitude modulation interaction.

From these observations of the spatio–temporal structure, one can reconstruct an equivalent correlation value to quantify the apparent correlation that appears in figure 8. Figure 9(a) shows this correlation via the variations of $\Delta\langle u_s^2\rangle(x^+ = 0, y^+ = 18, \tau)$ along with the local large-scale variation, $\langle u\rangle_{0c}(0, 18, \tau)$. The strong correlation and the leading of the small-scale variance with respect to the large-scale event in the near-wall region is readily apparent (where the modulation effects lead the superposition effects in time near the wall in an Eulerian perspective). Also shown in figure 9 is the large-scale signature at the outer-'probe' location ($\langle u\rangle_{0c}(0, y_O, \tau)$). A '1-point' and '2-point' correlation between these trends can then be computed, similar to that described in §III B. Since the flow is streamwise homogenous, this correlation at $x^+ = 0$ can be streamwise-averaged to improve convergence. These coefficients are presented in figure 9(b) and the similar trends of these correlations to those presented in figure 4, for example, further emphasizes the equivalency between the two metrics of amplitude modulation. The '2-point' correlation coefficient is higher than that of '1-point' as expected from §III B and from literature [34, for example]. Further, previous studies have shown that the correlated variation in small-scale energy lead the large scales in time close to the wall. This trend, which was also evident in figure 8, is also readily seen here. The coefficients shown in figures 4(a,b) were obtained from correlations between two signals where as the same in figure 9b were derived from conditional averages. The two metrics offer different perspectives of the same phenomenon.

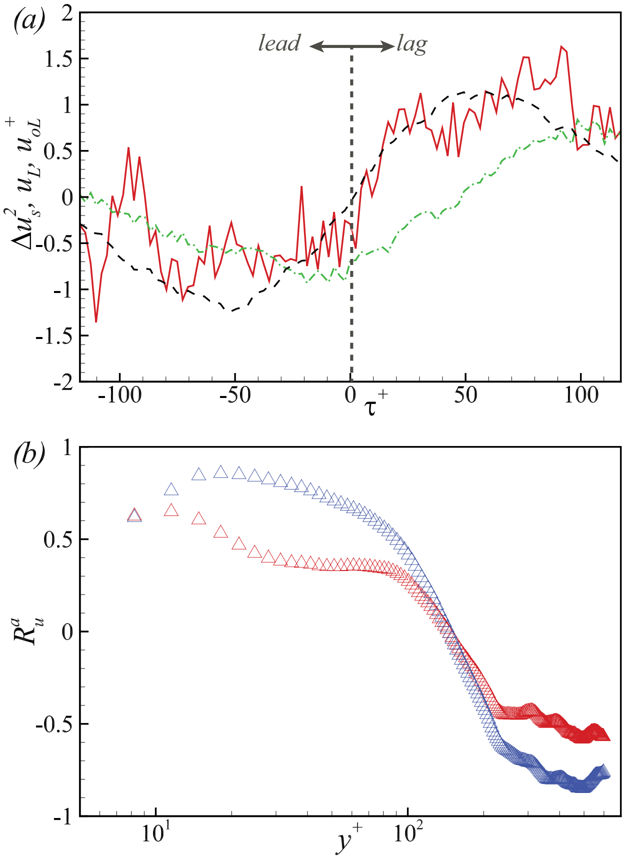

FIG. 9. (a) $\Delta\langle u_s^2\rangle(x^+ = 0, y^+ = 18, \tau)$ (*solid*), $\langle u\rangle_{0c}(0, 18, \tau)$ (*dash-dot*), and $\langle u\rangle_{0c}(0, y_O, \tau)$ (*dashed*). (b) '1-probe' and '2-probe' correlation coefficients similar to those in figure 4(a,b).

D. Effect of filtering mechanism

Finally, the definitions of large and small scales in §IV A (Eqns. 3 and 4) were used owing to the simplicity in scale separation. It can otherwise be seen as the application of a smoothing top-hat filter to demarcate the two interacting scales. The preceding analysis can also be undertaken by application of a sharp-spectral filter instead of ensemble averaging. Doing so provides an alternative decomposition of the scales with a different spectral signature of the cut-off filter. With the conditional ensemble of fields $[u_{0c}]_i$, we can define a new definition of large and small scales as

$$\tilde{u}_L(x, y, \tau) = \langle \mathcal{F}_{LP}(u_{0c}) \rangle \tag{6}$$

$$\tilde{u}_s^2(x, y, \tau) = \langle (u_{0c} - \mathcal{F}_{LP}(u_{0c}))^2 \rangle . \tag{7}$$

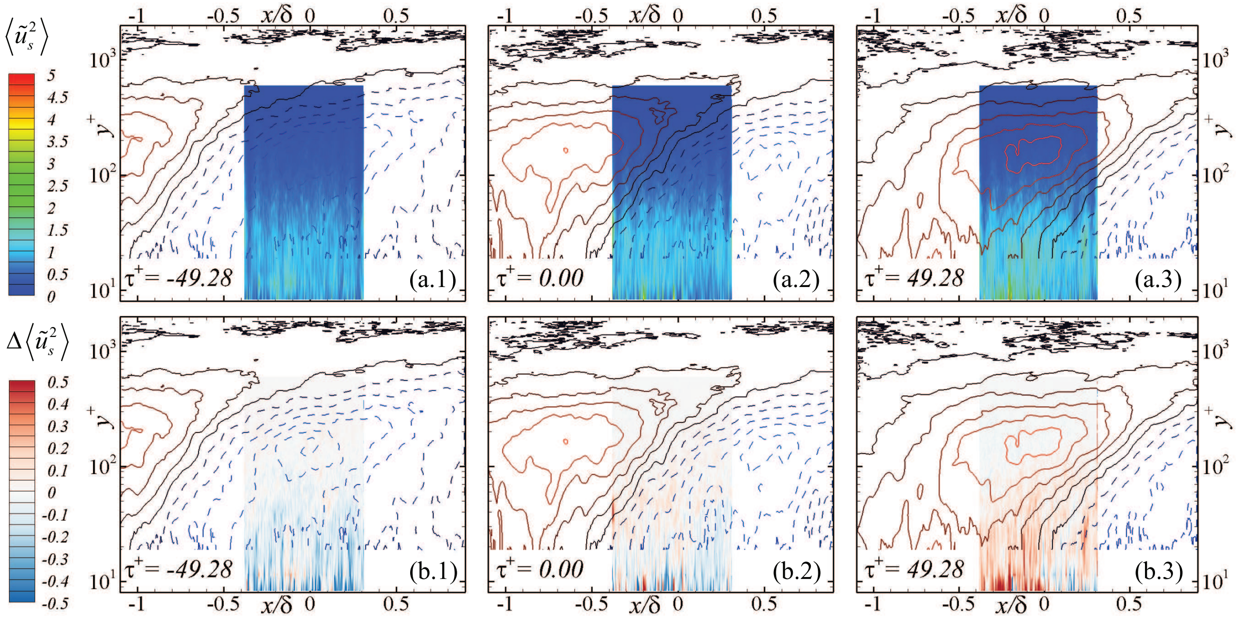

FIG. 10. Same as figure 8, but for large and small scales defined by a sharp-spectral filter. Please see video uploaded as supplemental material [77] which illustrates the full time evolution of the results presented in this figure.

Here, $\mathcal{F}_{LP}$ is a sharp-spectral low-pass filter with a cut-off wavelength $\lambda_c = 0.7\delta$ applied in the streamwise direction and $\tilde{(\cdot)}$ corresponds to filtered quantities. This filter length is slightly smaller than the streamwise extent of sFOV.

From eqns. 6 and 7, one can investigate the large- and small-scale evolution, along with the discrepancy similar to that performed in section IV C. This evolution at the three times corresponding to $\tau = \tau_{\downarrow}, 0$, and $\tau_{\uparrow}$ is present in figure 10 for streamwise components of these quantities. Besides slight differences in the finer structure of the two scales, the evolution and the correlation between them is strikingly similar to that seen in figure 8. This similarity is expected, as the choice of filtering method for scale decomposition should not have a significant effect on the scale interactions computed [75].

V. CONCLUSIONS

High-frame-rate PIV measurements, utilizing two PIV FOVs to ensure a high dynamic range, were performed in the streamwise–wall-normal plane in a refractive index-matched flow facility. This data was used to study IOIs in a smooth-wall turbulent boundary layer in a spatio–temporal sense.

After establishing the boundary layer and turbulence characteristics, point-wise analytics in a temporal-only analysis were employed to demonstrate that well-resolved, high-frame-rate PIV is indeed capable of capturing modulation effects that have only heretofore been experimentally studied via hot-wire measurements [1, 10, 22, 34]. Amplitude modulation was identified in both the streamwise and wall-normal velocities using single-, two-, and multi-point correlation coefficients, in agreement with similar observations in the literature [26, 42]. However, weaker signatures of frequency modulation were found, with a distinctive behavior in the wall-normal velocity. The FM coefficient of the streamwise velocity was found to be weaker in the current study compared to that reported using hot-wire measurements [1, 34]. More surprisingly, the FM coefficient of the wall-normal velocity was found to decay close to the wall unlike that of its AM counterpart, which is more significant in magnitude. This behavior is suspected to be due to increased sensitivity of FM correlation coefficients to noise, finite sub-pixel accuracy and spatial averaging inherent to PIV measurements, particularly close to the wall. It is important to consider these caveats when the FM trends in wall-normal velocity are considered. To the best of our knowledge, this work is the first to study attributes of FM in the wall-normal velocity component, so additional studies are required to comment further on this behavior.

Conditional averages revealed the spatial signature of the large scales and that modulation in small-scale energy occurred relative to the convecting large scales with a time/spatial delay, lending support to similar observations made in hot-wire amplitude modulation analysis. The present two-velocity component data allowed the exploration of such processes with the wall-normal velocity component, and a similar relationship was observed. The supplemental video for figure 8 highlights this mean structure of correlated streamwise and wall-normal turbulence intensity in space and time. Finally, to ensure that this structure is not an artifact of the spectral characteristics of the conditional averaging, a spectral-filter of turbulent fluctuations based on streamwise wavenumber was also employed to decompose the small- and large-scale fields and compute the average structures.

Taken together, the present analysis revealed a similar structure of IOIs as the inclined nature of the schematic proposed by Baars *et al.* [1], De Silva *et al.* [52] and Baars *et al.* [24]. Using a pair of hot-wires and investigating the temporal signatures of large scales and small scales embodied in streamwise velocity, Baars *et al.* [1, 24] proposed that the former lead the amplitude and frequency modulations imparted on the latter. Similar structure inferred from streamwise velocity was also shown by De Silva *et al.* [52] using high spatial-resolution, but temporally uncorrelated, PIV. In other words, the large scales are inclined in the streamwise direction and the amplitude and frequency modulations of the small scales trail the large scales in time. Similar conclusions regarding this interaction structure were observed over rough walls by Pathikonda and Christensen [34], highlighting the robustness of the same. These characteristics are clearly evident in the data presented here, specifically in figure 8, where the aforementioned inclination and the temporal lag from a perspective of a stationary probe are clear. Of interest, the spatial character of the 'average' large scale is quite reminiscent of a typical instantaneous large-scale structure often seen in the streamwise–wall-normal plane of wall turbulence. While this lag was observed as a temporal separation in the earlier studies based on hot-wire probes and inferred as a spatial separation using Taylor's hypothesis, the current study shows this behavior in a more direct way using spatially- and temporally-resolved PIV data. An equivalent correlation between the scales based on the conditional-averaging results was also proposed, using the temporal resolution of these averaged descriptions.

Finally, the current work demonstrates that a well-resolved, high-frame-rate PIV measurement is capable of capturing the signatures of IOIs, and that this data can be exploited to study the spatio–temporal characteristics of these interactions. In particular, while these measurements show consistency with previous findings based on point-wise measurements, they also highlighted additional details on their spatial structure in decoupling the spatial and temporal parts without the need for Taylor's hypothesis.

ACKNOWLEDGMENTS

This work is supported by the Air Force Office of Scientific Research under Grant No. FA9550-14-1-0101.

---

[1] W. J. Baars, K. M. Talluru, N. Hutchins, and I. Marusic, "Wavelet analysis of wall turbulence to study large-scale modulation of small scales," Exp. Fluids **56**, 1–15 (2015).

[2] M. Gad-el Hak and P. R. Bandyopadhyay, “Reynolds number effects in wall-bounded turbulent flows,” Appl. Mech. Rev **47**, 307–365 (1994).

[3] J.C. Klewicki, “Reynolds number dependence, scaling, and dynamics of turbulent boundary layers,” Journal of Fluids Engineering **132**, 094001 (2010).

[4] A. J. Smits, B. J McKeon, and I. Marusic, “High–reynolds number wall turbulence,” Annual Review of Fluid Mechanics **43**, 353–375 (2011).

[5] F. H. Clauser, “The turbulent boundary layer,” Adv. Appl. Mech. **4**, 1–51 (1956).

[6] J. B. Balakumar and R. J. Adrian, “Large-and very-large-scale motions in channel and boundary-layer flows,” Phil. T. Roy. Soc. A **365**, 665–681 (2007).

[7] R. J. Adrian, “Hairpin vortex organization in wall turbulence a,” Physics of Fluids **19**, 041301 (2007).

[8] B. Ganapathisubramani, E. K. Longmire, and I. Marusic, “Characteristics of vortex packets in turbulent boundary layers,” J. Fluid Mech. **478**, 35–46 (2003).

[9] N. Hutchins and I. Marusic, “Evidence of very long meandering features in the logarithmic region of turbulent boundary layers,” J. Fluid Mech. **579**, 1–28 (2007).

[10] R. Mathis, N. Hutchins, and I. Marusic, “Large-scale amplitude modulation of the small-scale structures in turbulent boundary layers,” J. Fluid Mech. **628**, 311–337 (2009).

[11] K. N. Rao, R. Narasimha, and B. M. A. Narayanan, “The bursting phenomenon in a turbulent boundary layer,” J. Fluid Mech. **48**, 339–352 (1971).

[12] P. R. Bandyopadhyay and A. K. M. F. Hussain, “The coupling between scales in shear flows,” Phys. Fluids **27**, 2221–2228 (1984).

[13] A. A. Townsend, *The structure of turbulent shear flow* (Cambridge University Press, 1976).

[14] R. J. Adrian, C. D. Meinhart, and C. D. Tomkins, “Vortex organization in the outer region of the turbulent boundary layer,” Journal of Fluid Mechanics **422**, 1–54 (2000).

[15] K. T. Christensen and R. J. Adrian, “Statistical evidence of hairpin vortex packets in wall turbulence,” J. Fluid Mech. **431**, 433–443 (2001).

[16] V. K. Natrajan and K. T. Christensen, “The role of coherent structures in subgrid-scale energy transfer within the log layer of wall turbulence.” Phys. Fluids **18**, 065104 (2006).

[17] K. C. Kim and R. J. Adrian, “Very large-scale motion in the outer layer,” Phys. Fluids **11**, 417–422 (1999).

[18] R. Mejia-Alvarez, Y. Wu, and K. T. Christensen, “Observations of meandering superstruc-

tures in the roughness sublayer of a turbulent boundary layer," Int. J. Heat Fluid Fl. **48**, 43–51 (2014).

[19] N. Hutchins and I. Marusic, "Large-scale influences in near-wall turbulence," Phil. T. Roy. Soc. A **365**, 647–664 (2007).

[20] K. M. Talluru, R. Baidya, N. Hutchins, and I. Marusic, "Amplitude modulation of all three velocity components in turbulent boundary layers," J. Fluid Mech. **746**, R1 (2014).

[21] R. Mathis, I. Marusic, S. I. Chernyshenko, and N. Hutchins, "Estimating wall-shear-stress fluctuations given an outer region input," Journal of Fluid Mechanics **715**, 163 (2013).

[22] R. Mathis, N. Hutchins, and I. Marusic, "A predictive inner–outer model for streamwise turbulence statistics in wall-bounded flows," J. Fluid Mech. **681**, 537–566 (2011).

[23] I. Marusic, R. Mathis, and N. Hutchins, "Predictive model for wall-bounded turbulent flow," Science **329**, 193–196 (2010).

[24] W. J. Baars, N. Hutchins, and I. Marusic, "Spectral stochastic estimation of high-reynolds-number wall-bounded turbulence for a refined inner-outer interaction model," Physical Review Fluids **1**, 054406 (2016).

[25] W. J. Baars, N. Hutchins, and I. Marusic, "Reynolds number trend of hierarchies and scale interactions in turbulent boundary layers," Phil. Trans. R. Soc. A **375**, 20160077 (2017).

[26] M. Bernardini and S. Pirozzoli, "Inner/outer layer interactions in turbulent boundary layers: a refined measure for the large-scale amplitude modulation mechanism," Phys. Fluids **23**, 061701 (2011).

[27] R. Mathis, I. Marusic, N. Hutchins, and K. R. Sreenivasan, "The relationship between the velocity skewness and the amplitude modulation of the small scale by the large scale in turbulent boundary layers," Phys. Fluids **23**, 121702 (2011).

[28] S. Duvvuri and B. J. McKeon, "Triadic scale interactions in a turbulent boundary layer," J. Fluid Mech. **767**, R4 (2015).

[29] M. Guala, M. M. Metzger, and B. J. McKeon, "Interactions within the turbulent boundary layer at high reynolds number," J. Fluid Mech. **666**, 573–604 (2011).

[30] D. Chung and B. J. McKeon, "Large-eddy simulation of large-scale structures in long channel flow," J. Fluid Mech. **661**, 341–364 (2010).

[31] N. Hutchins, J. P. Monty, B. Ganapathisubramani, H. C. Ng, and I. Marusic, "Three-dimensional conditional structure of a high-reynolds-number turbulent boundary layer," J.

Fluid Mech. **673**, 255–285 (2011).

[32] B. Ganapathisubramani, N. Hutchins, J. P. Monty, D. Chung, and I. Marusic, “Amplitude and frequency modulation in wall turbulence,” J. Fluid Mech. **712**, 61–91 (2012).

[33] D. T. Squire, W. J. Baars, N. Hutchins, and I. Marusic, “Inner–outer interactions in rough-wall turbulence,” Journal of Turbulence **17**, 1159–1178 (2016).

[34] G. Pathikonda and K. T. Christensen, “Inner–outer interactions in a turbulent boundary layer overlying complex roughness,” Phys. Rev. Fluids **2**, 044603 (2017).

[35] G. Pathikonda, *Inner-outer interactions in a rough-wall turbulent boundary layer*, Ph.D. thesis, University of Illinois at Urbana-Champaign (2017).

[36] K. Blackman and L. Perret, “Non-linear interactions in a boundary layer developing over an array of cubes using stochastic estimation,” Physics of Fluids **28** (2016).

[37] J. Basley, L. Perret, and R. Mathis, “Spatial modulations of kinetic energy in the roughness sublayer,” Journal of Fluid Mechanics **850**, 584–610 (2018).

[38] S. Duvvuri and B. J. McKeon, “Nonlinear interactions isolated through scale synthesis in experimental wall turbulence,” Phys. Rev. Fluids **1**, 032401 (2016).

[39] A. Dróżdż, W. Elsner, and S. Drobniak, “Scaling of streamwise reynolds stress for turbulent boundary layers with pressure gradient,” European Journal of Mechanics-B/Fluids **49**, 137–145 (2015).

[40] S. Pirozzoli, M. Bernardini, and P. Orlandi, “Large-scale motions and inner/outer layer interactions in turbulent couette–poiseuille flows,” Journal of Fluid Mechanics **680**, 534–563 (2011).

[41] D. Fiscaletti, B. Ganapathisubramani, and G. E. Elsinga, “Amplitude and frequency modulation of the small scales in a jet,” J. Fluid Mech. **772**, 756–783 (2015).

[42] S. Wu, K.T. Christensen, and C. Pantano, “Modeling smooth- and transitionally rough-wall turbulent channel flow by leveraging inner-outer interactions and principal component analysis,” Journal of Fluid Mechanics **863**, 407–453 (2019).

[43] W. Sidebottom, O. Cabrit, I. Marusic, C. Meneveau, A. Ooi, and D. Jones, “Modelling of wall shear-stress fluctuations for large-eddy simulation,” in *Proc. 19th Australasian Fluid Mechanics Conf., Melbourne, Australia* (2014).

[44] W. Anderson, “Amplitude modulation of streamwise velocity fluctuations in the roughness sublayer: evidence from large-eddy simulations,” J. Fluid Mech. **789**, 567–588 (2016).

[45] A. Awasthi and W. Anderson, “Numerical study of turbulent channel flow perturbed by spanwise topographic heterogeneity: Amplitude and frequency modulation within low-and high-momentum pathways,” Physical Review Fluids **3**, 044602 (2018).

[46] S. I. Chernyshenko, I. Marusic, and R. Mathis, “Quasi-steady description of modulation effects in wall turbulence,” arXiv preprint arXiv:1203.3714 (2012).

[47] C. Zhang and S. I. Chernyshenko, “Quasisteady quasihomogeneous description of the scale interactions in near-wall turbulence,” Phys. Rev. Fluids **1**, 014401 (2016).

[48] S. Chernyshenko, C. Zhang, H. Butt, and M. Beit-Sadi, “A large-scale filter for applications of qsqh theory of scale interactions in near-wall turbulence,” Fluid Dynamics Research (2018).

[49] C. J. Keylock, B. Ganapathasubramani, J. P. Monty, N. Hutchins, and I. Marusic, “The coupling between inner and outer scales in a zero pressure boundary layer evaluated using a hölder exponent framework,” Fluid Dynamics Research **48**, 021405 (2016).

[50] B. J. McKeon, “The engine behind (wall) turbulence: perspectives on scale interactions,” Journal of Fluid Mechanics **817** (2017).

[51] R. Hu and X. Zheng, “Energy contributions by inner and outer motions in turbulent channel flows,” Physical Review Fluids **3**, 084607 (2018).

[52] CM De Silva, EP Gnanamanickam, C Atkinson, NA Buchmann, N Hutchins, J Soria, and I Marusic, “High spatial range velocity measurements in a high reynolds number turbulent boundary layer,” Physics of fluids **26**, 025117 (2014).

[53] T. B. Nickels, I. Marusic, S. Hafez, N. Hutchins, and M. Chong, “Some predictions of the attached eddy model for a high reynolds number boundary layer,” Philosophical Transactions of the Royal Society of London A: Mathematical, Physical and Engineering Sciences **365**, 807–822 (2007).

[54] M. V. Zagarola and A. J. Smits, “Mean-flow scaling of turbulent pipe flow,” Journal of Fluid Mechanics **373**, 33–79 (1998).

[55] P. Vincenti, J. Klewicki, C. Morrill-Winter, C. M. White, and M. Wosnik, “Streamwise velocity statistics in turbulent boundary layers that spatially develop to high reynolds number,” Experiments in fluids **54**, 1629 (2013).

[56] R. Örlü, T. Fiorini, A. Segalini, G. Bellani, A. Talamelli, and H. P. Alfredsson, “Reynolds stress scaling in pipe flow turbulence– first results from ciclope,” Phil. Trans. R. Soc. A **375**, 20160187 (2017).

[57] M. M. Metzger, *Scalar dispersion in high Reynolds number turbulent boundary layers*, Ph.D. thesis, Ph. D. thesis, University of Utah, Salt Lake City, UT (2002).

[58] D. J. C. Dennis and T. B. Nickels, "On the limitations of taylor's hypothesis in constructing long structures in a turbulent boundary layer," Journal of Fluid Mechanics **614**, 197–206 (2008).

[59] D. J. C. Dennis and T. B Nickels, "Experimental measurement of large-scale three-dimensional structures in a turbulent boundary layer. part 2. long structures," Journal of Fluid Mechanics **673**, 218–244 (2011).

[60] O. Uzol, Y-C. Chow, J. Katz, and C. Meneveau, "Unobstructed particle image velocimetry measurements within an axial turbo-pump using liquid and blades with matched refractive indices," Experiments in Fluids **33**, 909–919 (2002).

[61] J. Hong, J. Katz, and M. P. Schultz, "Near-wall turbulence statistics and flow structures over three-dimensional roughness in a turbulent channel flow," Journal of Fluid Mechanics **667**, 1–37 (2011).

[62] T. Kim, G. Blois, J. L. Best, and K. T. Christensen, "Experimental study of turbulent flow over and within cubically packed walls of spheres: Effects of topography, permeability and wall thickness," International Journal of Heat and Fluid Flow **73**, 16–29 (2018).

[63] N. Bristow, G. Blois, J. L. Best, and K. T. Christensen, "Turbulent flow structure associated with collision between laterally offset, fixed-bed barchan dunes," Journal of Geophysical Research: Earth Surface (2018), 10.1029/2017JF004553.

[64] K. Chauhan, H. M. Nagib, and P. A. Monkewitz, "On the composite logarithmic profile in zero pressure gradient turbulent boundary layers," in *Proc. 45th AIAA Aerospace Sciences Meeting, Paper No. AIAA*, Vol. 532 (2007) pp. 1–18.

[65] R. Örlü and P. Schlatter, "Comparison of experiments and simulations for zero pressure gradient turbulent boundary layers at moderate reynolds numbers," Experiments in fluids **54**, 1547 (2013).

[66] P. Schlatter and R. Örlü, "Assessment of direct numerical simulation data of turbulent boundary layers," Journal of Fluid Mechanics **659**, 116 (2010).

[67] H. C. Ng, J. P. Monty, N. Hutchins, M. Chong, and I. Marusic, "Comparison of turbulent channel and pipe flows with varying Reynolds number," Exp. Fluids **51**, 1261–1281 (2011).

[68] Z. Harun, J. P. Monty, R. Mathis, and I. Marusic, "Pressure gradient effects on the large-scale

structure of turbulent boundary layers," Journal of Fluid Mechanics **715**, 477–498 (2013).

[69] S. Hoyas and J. Jiménez, "Scaling of the velocity fluctuations in turbulent channels up to re τ= 2003," Physics of Fluids **18**, 011702 (2006).

[70] G. Eitel-Amor, R. Örlü, and P. Schlatter, "Simulation and validation of a spatially evolving turbulent boundary layer up to reθ= 8300," International Journal of Heat and Fluid Flow **47**, 57–69 (2014).

[71] R. J. Adrian, "On the role of conditional averages in turbulence theory," Turbulence in Liquids **1**, 323–332 (1977).

[72] E. Dogan, R. Örlü, D. Gatti, R. Vinuesa, and P. Schlatter, "Quantification of amplitude modulation in wall-bounded turbulence," Fluid Dynamics Research (2018).

[73] C. D. Meinhart and R. J. Adrian, "On the existence of uniform momentum zones in a turbulent boundary layer," Physics of Fluids **7**, 694–696 (1995).

[74] I. Jacobi and B. J. McKeon, "Phase relationships between large and small scales in the turbulent boundary layer," Exp. Fluids **54**, 1–13 (2013).

[75] J.A. Domaradzki and D. Carati, "A comparison of spectral sharp and smooth filters in the analysis of nonlinear interactions and energy transfer in turbulence," Physics of Fluids **19**, 085111 (2007).

[76] See Supplemental Material at [URL] for full time evolution of the large-scale – smalle-scale organization based on conditional averaging.

[77] See Supplemental Material at [URL] for full time evolution of the large-scale – smalle-scale organization based on spectral-filter.